QATAR UNIVERSITY

COLLEGE OF ARTS AND SCIENCES

CONTROLLED FABRICATION OF EFFICIENT POROUS MULTIFUNCTIONAL NANOCATALYSTS FOR THE GAS CONVERSION REACTIONS TO USABLE FUELS: A CLOSER STEP FOR COMMERCIALIZATION

BY

AHMED MOHAMED SHEHATA SOLIMAN

A Thesis Submitted to

the College of Arts and Sciences

in Partial Fulfillment of the Requirements for the Degree of

Masters of Science in Material Science and Technology

June 2020

COMMITTEE PAGE

The members of the Committee approve the Thesis of
Ahmed Soliman defended on 23/04/2020.

Dr. Aboubakr Abdullah
Thesis/Dissertation Supervisor

Dr. Mohamed Hassan
Committee Member

Dr. Abdul Shakoor
Committee Member

Dr. Kamel Eid
Committee Member

Approved:

Ibrahim AlKaabi, Dean, College of Arts and Sciences

ABSTRACT

SOLIMAN, AHMED, MOHAMED, Masters : June : 2020, Material Science and Technology

Title: Controlled Fabrication of Efficient Porous Multifunctional Nanocatalysts for the Gas Conversion Reactions to Usable Fuels: A closer Step for Commercialization

Supervisor ofThesis: Dr. Aboubakr, M. Abdullah. Hydro/Qatalum Chair Professor, Center for Advanced Materials, Qatar University.

Carbon-based (CNs) nanostructures attracted great attention in various conversion energy technologies, owing to their unique physicochemical properties such as high surface area, abundant active sites, and stability. Herein, we developed a facile approach for the rational fabrication of CNs nanostructures included MXene and Nitrogen enriched carbon capsules doped with metal atoms at the atomic level. The as-formed nanostructures possess outstanding properties such as massive surface area (x m_2 g^{-1}), accessible active sites. Although the great progress in the development of Nano-catalysis for gas conversion reactions, it remains a great chance to find efficient, durable, cost-effective, and selective catalysts work under mild reaction conditions such as room temperature and atmospheric pressure. Unlike other catalysts reported elsewhere, the proposed catalysts herein possess outstanding inbuilt properties of atomic-doped carbon-based materials such as great thermal/chemical stability, high surface area, massive adsorption sites for gases and their ability to inherently generate oxygenated or hydrogenated species which accelerate the reaction kinetics under low temperature (thermally) and low potential window (electrochemically). Also, these materials can be prepared from different abundant and inexpensive materials.

DEDICATION

This thesis is dedicated to my family, including my father, mother, wife, and kids, for their great support all my life. Also, I greatly appreciate my supervisors for their support during my master's study. I would like to express a special Thanks to my supervisor Dr. Aboubakr who dedicated his time for helping, supporting, and guiding me. Lastly, all my appreciation for my father and mother.

ACKNOWLEDGMENTS

I greatly appreciate the Gas processing center (GPC) at Qatar University for allowing me to use the GPC-facilities during my study. I also greatly appreciate the CAS College, CLU, and CAM departments for allowing me to use their facilities during the study. Finally, I would like to express my great thanks to the MATS program Team at Qatar University for their support and encouragement.

TABLE OF CONTENTS

List of Tables

LIST OF FIGURES

Chapter 1: Introduction

The gas conversion reactions, especially CO and CO_2, are important in different kinds of multidisciplinary basics, industrial, and environmental applications.[1-4] This attracted numerous researchers to the synthesis of wide ranges of catalysis for controlled CO oxidation or CO_2 reduction, including but not limited metal-based, metal oxide-based, and metal-organic frameworks catalysts.[5, 6] Supported noble Metal-based catalysts such as Pt, Pd, Au, Ag, Ir, and Ru or transition metals such as Cu, Co, Zn, and Al, all in all, are well known with their impressive electrochemical and/or thermal gas conversion efficiency, owing to their great ability to CO/CO_2 gases under ambient conditions.[7-9] [10] This is in addition to their ability to facilitating the adsorption/dissociation gases along with generating various oxygenated or hydrogenated species to facilitate the reaction kinetics. [11-13]

For instance, Pd on SiO_2 catalyst showed great catalytic performance for CO oxidation than that of $Pd_1Au_{3.4}$ on SiO_2, Pd_2Au_1 on SiO_2, and $Pd_1Au_{1.6}$ on SiO_2 catalysts, respectively.[14] Another factor for improving the catalytic performance of the metal-based catalyst, is their combination in the form of alloys, due to their electronic effect and bifunctional mechanisms. [15-17] Likewise, Pd_7Cu_1-TiO_2 allowed photo-electrochemically conversion of CO_2 to CH_4 (96 % efficiency) with a rate of 19.6 μmol g_{cat}^{-1} h^{-1} .[18] CO_2 was converted to methanol electrochemically on Pd-Cu catalysts.[19] The type of support is also among the most important factor for improving the catalyst performance of metal-catalysts in CO/CO_2 conversion reactions due to their electronic interaction that tunes the adsorption of reaction products/and/or intermediate species results in high activity and stability.[20, 21] Despite the great advances made in developing metal on supporter catalysts for CO/CO_2 conversion, their high cost, unsuitable selectivity, less-durability on the long term of remain

a grand difficulties on the large-scale applications. Also, most previous reported catalysts were in the form nanoparticles over supporter which suffer from an investable aggregation or detachment and poisoning during CO/CO_2 conversion reactions. In the presented proposal we will focus on controlled fabrication of novel porous multifunctional carbon-based (CNs) nano catalysts with different shapes atomically functionalized with various metals and/or non-metals for the efficient and selective conversion of CO/CO_2 gasses to usable hydrocarbon fuels under ambient reaction conditions. Multifunctional porous CNs with multiple dimensions are prepared over traditional metal-catalysts, due to their high surface area to volume ratio, great stability chemically or thermally, and massive accessible active sites. [22-24] This is beside the easy of preparation CNs materials from different inexpensive resources on the earth and can be easily handled or stored. Also, CNs materials with various metals and/or non-metal traces in the form of atomic functionalities posses additional benefits, like great active catalysis sites and stability against degradation or detachment. [22-24] Meanwhile, the atomic functionalization allows using a very low amount of the metal or non-metals (nearly 1-3 wt %), which are highly required not only for reducing the cost but also to decrease the consumption of expensive and rare metals. [22-24] There very few articles about using CNs- materials with atomic functionalities that focused only on one-dimension structure and CO oxidation. [4, 25-29] In addition, for the first time, we will teste the catalytic performance of CNs-based catalysts electrochemically, photo-electrochemically, and thermally. The selectivity will be adjusted by changing the type of atomic functionalities.

1.1 Theoretical Concerns / Situating The Study In The Field

Even though the great progress in the development of Nanocatalysis for gas conversion reactions, it remains a great chance to find efficient, durable, cost-effective, and

selective catalyst work under mild reaction conditions such as room temperature and atmospheric pressure. Replacing the noble-metal based catalyst in the electrochemical CO/CO_2 conversion reactions or transition-metals in the thermal CO/CO_2 conversion remains a great challenge. We will combine the unique physical and chemical properties of porous multifunctional CNs materials with the impressive inbuilt catalytic properties of atomic metal functionalities to allow the effective, durable, selective, and low-cot CO/CO_2 conversion to useful hydrocarbons.

1.2 Research Objectives

The presented thesis is dedicated to controlling the synthesis of novel porous multifunctional carbon-based catalytic nanosystems contains various metals and/or non-metals at the atomic level for the conversion of CO and CO_2 gasses to liquid hydrocarbon fuels. Unlike other catalyst reported elsewhere, the proposed catalysts herein possess outstanding inbuilt properties of atomic-doped carbon-based materials such as great thermal/chemical stability, high surface area, massive adsorption sites for gases and their ability to inherently generate oxygenated or hydrogenated species which accelerate the reaction kinetics under low temperature (thermally) and low potential window (electrochemically). Also, these materials can be prepared from different abundant and inexpensive materials. The proposed catalyst will be characterized using various techniques such as TEM, SEM, XRD, and XPS. Meanwhile, the catalytic activity, durability, and selectivity can be controlled through the type of metal/non-metal functionalities. The gas conversion reaction will be invested thermally, electrochemically, and photo-electrochemically. Moreover, the reaction mechanisms and kinetics will be explained deeply.

Chapter 2: Background/Literature Review

2.1 Method For Gas Conversion Reactions

2.1.1 Electrochemical

The electrochemical measurements will be examined using a Gamry electrochemical analyzer (reference 3000, Gamry Co., USA) in the presence of a three-electrode cell, including counter, reference, and working electrodes.[4] The working electrode will be functionalized with a known amount of each catalyst via drop-casting and then left to dry before being covered with a layer of Nafion. The electrodes should be left to dry before any usage in the electrochemical reactions. The CO or CO_2 gas mixture with different compositions will be purged in the electrolytes during measurements. Different electrochemical tests will be used, such as cyclic voltammograms (CVs), linear sweep voltammograms (LSVs), chronometry (CA), impedance spectroscopy (EIS), and Tafel plot will be measured in differ electrolytes solutions saturated and unsaturated with gas mixtures. All the required calculations, such as electrochemical surface area, Faradic efficiency, and Tafel slope, will be estimated after the measurements using their standard methods.

The products produced from the gas conversion reactions have been analyzed using two techniques; the first one is Perkin Elmer Clarus 680 - GC-MS with TurboMatrix Headspace Sampler and TotalChrom Workstation Software. The second technique Instrument has been used for formic acid quantification was Water Acquity UPLC with UV at 210 nm, and the column used for separation was Agilent C18 4um particle size, 4.6 x 150mm dimensions at ambient temperature. Also specific Isocratic elution used at constant flow rate 1 ml/min of sulfate buffer (1 mmol/L H_2SO_4+ 8 mmol/L Na_2SO_4 (pH 2.8)) to be easily separate the formic acid.

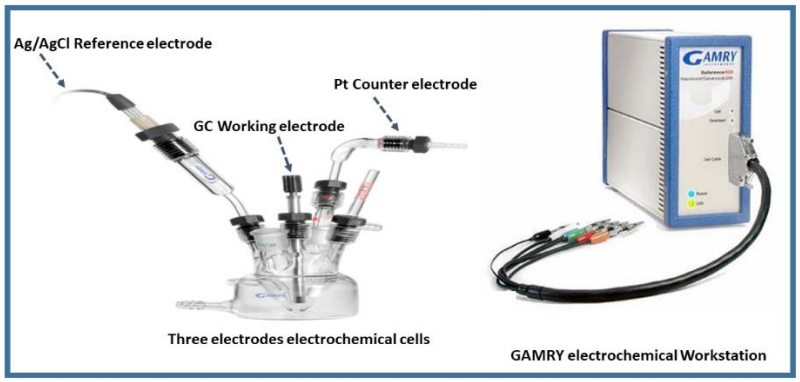

Figure 1. The electrochemical setup measurements for CO_2 conversion

2.1.2 Photoelectrochemcial

The three-electrodes cell will be sued but with using a fluorine-doped tin oxide plate as a working electrode. [5][4] The as-formed catalyst will be deposited over the tin sheet and then covered with a Nafion layer before measurements. All the testes in electrochemical sections such as CVs, LSV, Tafel, and EIS should be measured under light sources such as zone-free xenon lamp (100 mW/cm^2) (Figure 2). The products produced from the gas conversion reactions were analyzed using GC-MS and UPLC with UV.

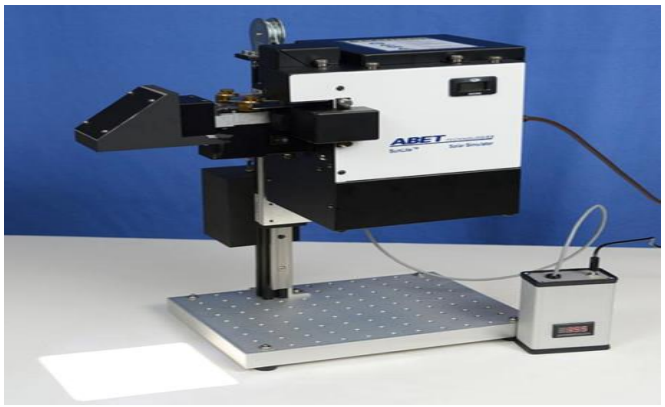

Figure 2. UV Solar Simulator instrument

2.1.3 Thermal Catalytic Reactions

Types of reactor [30, 31].

1- Fixed bed reactor

2- Slurry reactor

3- Fluidized reactor

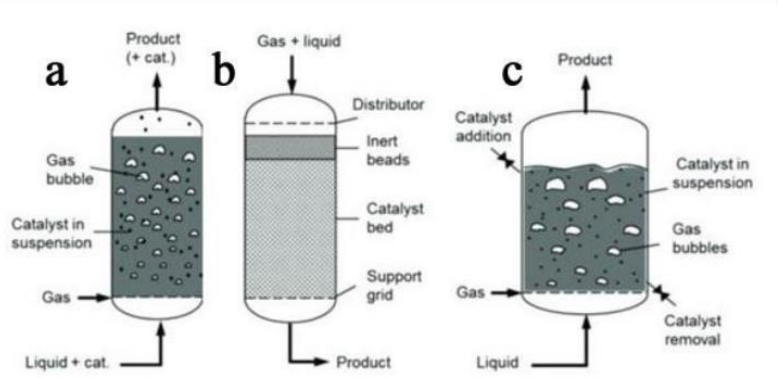

Figure 3 shows the main differences between the slurry reactor (a), fixed bed reactor (b) and fluidized reactor (c) **[31]**

A fixed bed reactor is a cylindrical tube filled with catalyst pellets with reactants flowing through the bed and being converted into products. The catalyst may have multiple configurations, including one large bed, several horizontal beds, several parallel packed tubes, multiple beds in their own shells [31].

Slurry reactors are similar to fluidized-bed reactors in that a gas is passed through a reactor containing solid catalyst particles suspended in a fluid. In slurries, the catalyst is suspended in a liquid, whereas in fluidized beds, the suspending fluid is the reacting gas itself.

Fluidized bed reactors are heterogeneous catalytic reactors in which the mass of catalyst is fluidized. This allows for extensive mixing in all directions. A result of the mixing is excellent temperature stability and increased mass-transfer and reaction rates [32].

In our study, The thermal reaction was measured using the as-synthesized materials in a fixed bed Hastelloy tubular reactor equipped with a GC system designed in our lab. [6] A known amount of each catalyst (50-100 mg) will be put in the reactor and partially heated under hydrogen and under heating by 5 ^{o}C/min till 250 ^{o}C for the activation of the as-obtained before the testing. Then, the catalysts will be subjected to gas mixtures from H2 and CO_2 by a 3:1 ratio under continuous heating from the 200 ^{o}C to 300 ^{o}C. Various parameters will be changed, such as temperature, pressure, atmospheric conditions, to tailor the composition of the final products. The products produced from the gas conversion reactions were analyzed using GC-TCD and GC-MS.

2.2 Impact Of Gas Conversion Reactions

Worldwide

Reducing greenhouse gas emissions, especially CO_2 and CO, are of great importance all over the world due to their great hazard effect on humans, plans, and environmental as well as climate change. Table 1 shows the CO_2 emission per capita all over the word.[33] Intestinally, there are around 6 Arabian countries, including Qatar, Kuwait, United Arab Emirates, Bahrain, Saudi Arabia, Oman is among the top 10 countries in the highest CO_2 emission per capita around the world. Thus, the conversion of greenhouse gasses into useful hydrocarbons is among the most intriguing approaches. In particular, the continued global energy consumption peaked up substantially in the last decades, and it is expected to rise by more than 40 % in the coming 20 years, owing to the continued economic growth along with the overpopulation. This led to massive emissions of CO and CO_2 gases, which will rise again by around 15 % in the coming ten years (Table 1). To this end, over 100,000 million metric tons of CO and CO_2 gasses are emitted annually worldwide.

		2018	2017	2016	2015	2014	2013	2012	2011	2010	20(
1	Palau	57.95	57.02	1.94	56.14	1.72	1.64	1.51	1.56	103.08	87.
2	Qatar	38.19	39.33	38.52	39.42	38.47	38.43	39.35	39.07	39.11	49.
3	Trinidad and Tobago	26.19	26.28	25.72	26.73	27.26	27.06	25.49	27.49	29.15	23.
4	Kuwait	23.91	22.99	25.06	24.27	24.72	25.28	27.03	28.32	28.81	33.
5	United Arab Emirates	22.44	22.14	23.60	22.10	21.43	21.36	21.04	20.38	20.78	26.
6	Bahrain	21.85	23.41	17.10	24.61	16.77	16.21	15.18	15.38	23.24	26.
7	Saudi Arabia	18.63	19.18	16.01	19.29	16.07	15.52	15.59	15.54	17.44	14.
8	Estonia	18.62	17.67	17.10	15.07	16.20	17.53	15.31	15.22	16.59	14.
9	Oman	17.64	17.54	19.87	18.76	20.67	20.86	21.47	22.53	17.29	13.
10	Luxembourg	16.86	16.46	17.61	16.48	17.22	18.41	19.99	21.19	22.14	26.
11	Kazakhstan	16.80	15.03	12.88	14.58	13.77	15.28	14.68	15.99	14.43	11.
12	Australia	16.77	16.83	17.22	16.89	17.24	17.84	18.32	18.98	18.66	19.
13	United States	16.14	15.81	15.56	16.33	16.54	16.39	16.31	17.13	18.00	20.
14	Canada	16.08	16.25	18.62	16.41	19.69	19.80	19.79	19.86	16.56	17.
15	Brunei	15.96	15.88	18.14	15.59	16.79	17.51	17.85	18.95	18.94	14.
16	Turkmenistan	14.38	13.46	14.01	13.40	13.04	13.08	13.12	12.98	12.11	11.
17	Falkland Islands	13.59	13.15	16.69	13.02	15.92	15.79	14.40	14.40	8.19	5.6
18	South Korea	13.59	13.25	11.89	12.63	11.87	12.00	12.13	12.29	12.06	10.
19	Russia	12.14	11.73	11.54	11.78	11.90	12.41	12.63	12.58	11.63	11.
20	Iceland	12.10	12.14	11.82	11.60	11.54	11.23	11.07	11.05	11.47	10.
21	Taiwan	12.01	12.02	11.73	11.28	11.75	11.77	11.67	11.70	11.75	11.
22	Barbados	11.58	10.77	5.41	11.16	5.16	5.10	4.70	4.78	8.36	7.8

Table 1. The CO2 emission per capita for the highest 22 countries around the world.

The Arabian countries are in the top 10 in the highest CO_2 emission around the world due to the oil and gas industries as well. To this end, Qatar has the highest CO_2 emission per capita around the world. Meanwhile, Kuwait is the third in the highest CO_2 emission worldwide (Table 1). Qatar Hydro Qatar Aluminum company produces around 4,987,233 mt of CO_{2eq} (nearly 7.63 tons of CO_{2eq} per ton of aluminum) and is expected to go up by around 20 % in the coming ten years. In addition, there are around 1,319,563.000 cars in Qatar emit nearly 98,967.225 tons of CO annually. Thereby the successful conversion of CO and CO_2 into useful hydrocarbon fuels not only important environmentally but also economically and will be sustainable energy sources for Arabian countries.

2.3 Literature Review On Carbon-Based Catalysis For Gas Conversion Reaction

Carbon-base materials such as graphene, graphene oxide, and carbon nanotubes are widely used as support for metal-based catalysts in gas conversion reactions[34-37]. This is due to their great surface area, electron-rich density, and stability. However, it should be noticed that in this literature review, we focused only on the most advanced and hot carbon-based materials, which developed recently for the gas conversion reaction and rarely reported elsewhere[38]. This is including emphasizing the fabrication of nitrogen-enriched 1D graphitic carbon nanostructures doped atomically with binary metals at the atomic level for CO oxidation and CO_2 reduction thermally, electrochemically, and photoelectrochemically. This is in addition to the fabrication of MXene-based nanostructures for CO_2 reduction electrochemically, and photo-electrochemically. The preparation approaches, characterization tools, formation mechanisms were deeply explained.

2.3.1 MXene-Based Catalysis/Gas Conversion Reactions.

2.3.1.1 MXene Quantum Dots

A heterostructure was designed from 1D photoactive semiconductor (Cu_2O nanowires (NWs)) and 0D MXene quantum dot (Ti_3C_2 QD) through an electrostatic self-assembly mechanism to enhance the photocatalytic reduction of CO_2. Ti_3C_2 QD exhibit featured properties such as bandgap widening due to quantum confinement, better tunability in physicochemical properties, more abundant active edge sites, and better dispersibility [39]. A typical preparation of Ti_3C_2 using HF followed by a hydrothermal cutting for the Ti_3C_2 sheets forming Ti_3C_2 QD. Meanwhile, copper (Cu) mesh went through an anodization and calcination process, forming porous-Cu_2O nanowire NWs/Cu. The electrostatic self-assembly of Ti_3C_2 QDs/Cu_2O NWs/Cu heterostructure is formed by

tuning the surface charge of each Ti_3C_2 QDs and Cu_2O NWs/Cu with positive and negative charge using polyethyleneimine (PEI) and adding poly (sodium 4-styrene sulfonate) (PSS), respectively, (Figure 4). A porous surface structure of Cu_2O NWs was confirmed by FE-SEM (Figure 5a-b). Whereas (Figure 5c-d) and (Figure 5e-f) shows the conjunction rule of Ti_3C_2 QD and Ti_3C_2 sheets covering the porous surface while maintaining the overall structure of Cu_2O NWs. Three samples were prepared named, Ti_3C_2 QDs/Cu_2O NWs/Cu, Ti_3C_2 sheet/Cu_2O NWs/Cu, and Cu_2O NWs/Cu to evaluate their performance in a photocatalytic reduction for CO_2. The three Cu_2O-based photocatalysts exhibit a selective conversion for methanol (CH_3OH) for 6 hours Figure 6. Out of the prepared samples, Ti_3C_2 QDs/Cu_2O NWs/Cu stands with the highest yield of conversion (153.38 ppm cm^{-2}), which is 2.15 and 8.25 times of its counterpart (70.25 ppm cm^{-2}) and pristine (18.82 ppm cm^{-2}) catalyst, respectively.

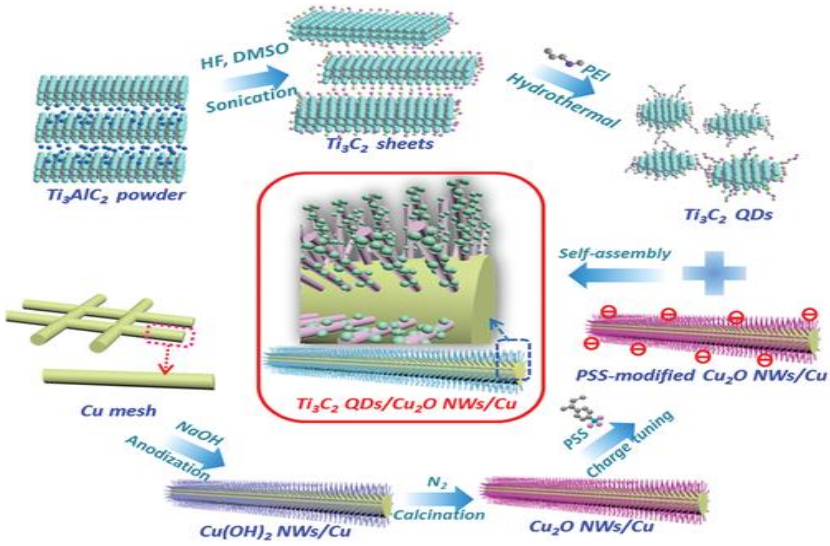

Figure 4 Schematic illustration for preparing Ti_3C_2 QDs and Ti_3C_2 QDs/Cu_2O NWs/Cu heterostructure. Adapted with copyright permission from WILEY 2018 [39].

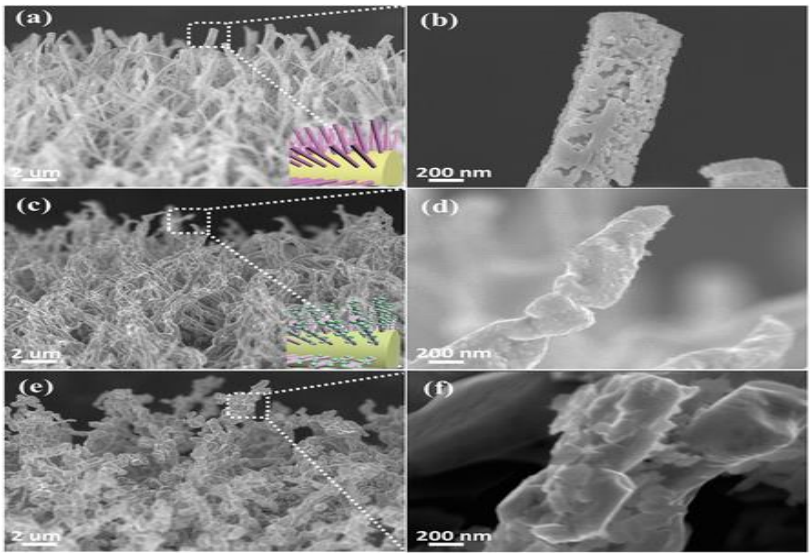

Figure 5 Field emission scanning electron microscopy images of a,b) Cu_2O NWs/Cu, c,d) Ti_3C_2 QDs/Cu_2O NWs/Cu, and e,f) Ti_3C_2 sheets/Cu_2O NWs/Cu heterostructures. Adapted with a copyright permission from [39].

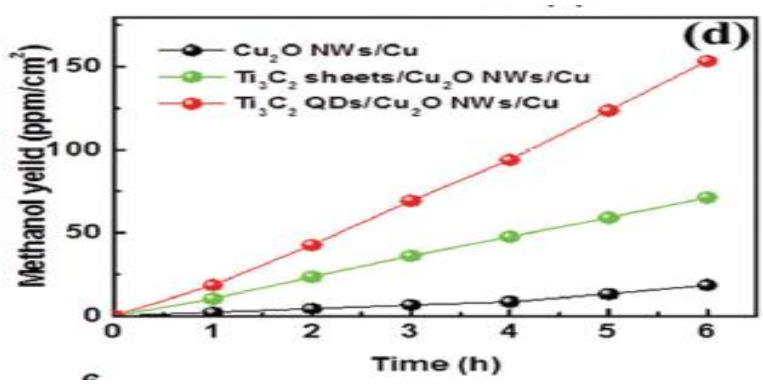

Figure 6 Yield of methanol as a function of time. Adapted with copyright permission from [39].

2.3.1.2 2D/2D Hetero-MXene.

A 2D/2D heterojunction of ultrathin Ti_3C_2/Bi_2WO_6 nanosheets was designed, as shown in (Figure 7). The aluminum was chemically removed from the Max phase by hydrofluoric acid, forming a multilayer of MXene (Ti_3C_2) [40]. Subsequently, the etched MXene was intercalated using dimethyl sulfoxide (DMSO) then exfoliated to form Ti_3C_2 nanosheets. One after the other, Bismuth (III) nitrate and Sodium tungstate-CTAB solutions were added to the MXene nanosheets undergoing a hydrothermal reaction to form the 2D/2D structure of Ti_3C_2/Bi_2WO_6. Such a usage of the unique 2D structure of MXene favors the fabrication of a 2D/2D heterostructure over its counterparts, forming 0D/2D and 1D/2D, endowing strong surface connection between the cocatalyst (MXene) and the photocatalyst (Bi_2WO_6). The intimate contact formation within the 2D/2D heterojunction further enhances the transference and separation of induced charge carriers. Owning to a crucial factor as strong physical and electronic coupling effect that enhances the photocatalytic efficiency, despite the decrease in surface area due to the stacking of the nanosheets. The photocatalytic performance for CO_2 reduction of the prepared samples was analyzed in a solar irradiation simulated medium. Both methane and methanol were the major photocatalytic products with a higher selectivity for methane as shown in (figure8a). The photocatalytic reduction of CO_2 from TB_2 shows a conversion rate of 1.7 µmol. g-1.h-1 for CH_4 and 0.44 µmol. g-1.h-1 CH_3OH which represents four and six folds of methane and methanol, respectively, in comparison with Bi_2WO_6. Gas chromatography-mass spectrometer (GC-MS) was applied to reveal the original source of carbon in the reaction products. Figure 8b&c shows 12-CH_4 and 13-CH_4 are the main products of 12-CO_2 and 13-Co_2, respectively. Furthermore, both the retention time and mass-to-charge ratio (m/z) of 12-CH4 are shorter than that of 13-CH4. The 2D/2D

heterojunction Ti_3C_2/Bi_2WO_6 shows a characteristic advantage such as a large interface and a short charge transfer distance that ease the transfer of the photo-induced electrons from the conductive band of the photocatalyst to the Ti_3C_2 surface. Not to mention, the addition of Ti_3C_2 to the photocatalyst increases the surface area and promote the CO_2 chemisorption.

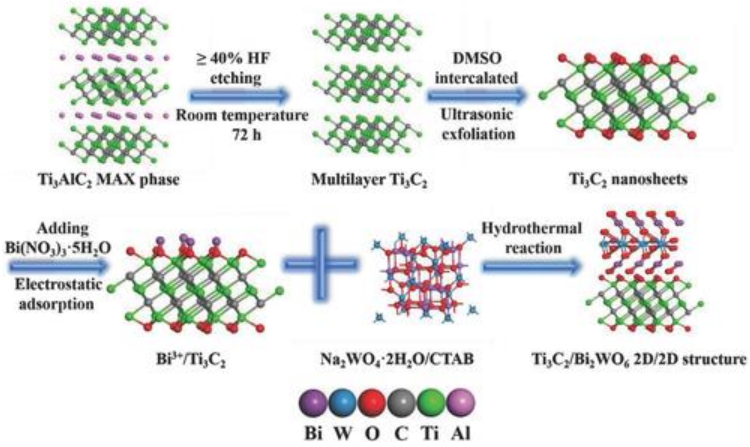

Figure 7 Schematic illustration of the synthetic process of 2D/2D heterojunction of ultrathin Ti_3C_2/Bi_2WO_6 nanosheets. Adapted with copyright permission from WILEY 2018 [40].

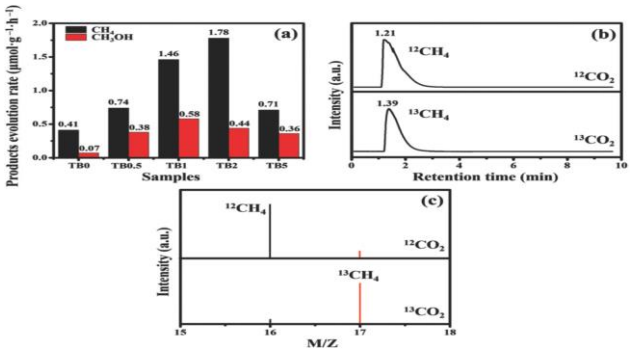

Figure 8 Photocatalytic activity of TB0 to TB5; b) GC-MS spectra over TB2 after irradiation for several hours with different carbon sources; c) GC-MS analysis of reaction products with 12C and 13C as carbon sources, respectively. Adapted with copyright permission from WILEY 2018 [40].

2.3.1.3 MXene -composite

In-Situ Growth of TiO_2 NPs grafted on the conductive surface of Ti_3C_2 was prepared via a fictile calcination method, allowing for a better intimate contact area compared to mechanically mixed materials [41]. The mass loading of TiO_2 NPs was tailored by variating the calcination temperature at 0, 350, 450, 550, and 650 °C, forming TT350, TT450, TT550, and TT650 samples, respectively. More importantly, the uniform size distribution of TiO2 nanoparticles is shown by SEM, forming a unique rice crust-like structure that is owned to the in-situ transformation of TiO_2 to Ti_3C_2 that can restrain the agglomeration and maintain this uniformity (Figure 9). Additionally, a lot of air voids found to be excited about TT550 as a result of the formation of CO_2 in the calcination process (Figure 9). However, the size of the air voids was found to be decreasing upon further increasing the calcination temperature (increasing TiO_2 content) since the particle size will be larger, in line with the specific surface area. Such behavior is attributed to a trade-off relation between the crystallinity and the particle size. The electrochemical measurements were performed on a three-electrode system while using a 0.5 Na2SO4 solution as an electrolyte. A significant photocurrent response for TT550 over the rest of the samples referring to the highest enhanced electron-hole transfer efficiency and lowest recombination rate. A distinctive response behavior for TT650 manifested by a spike upon exposure to light irradiation, due to a direct transfer of photoexcited electrons forms TiO_2 to the cathode. Unlike the rest of the samples that showed a curve response owned to electron-hole separation as the photoelectrons transferred to the cathode after passing through Ti_3C_2. The photocatalytic reduction of CO_2 for TiO_2/Ti_2C_3 composite was performed under the light. Among the three products, CH_4 was the most dominant product as it has the lowest reduction potential (-0.24 V) compared to CH_3OH (-0.38 V) and C_2H_5OH (-0.33

V) (Figure 10a). The general trend of methane production rate indicates the improved performance upon increasing the calcination temperature till 550° C. A deteriorated photocatalytic performance for TT650 owned to the non-attendance of Ti_3C_2 causing fast electron-hole recombination as well as a decrease in the surface area. The best sample TT550 showed a production rate (0.22 µmol h -1) 3.7 times higher than the commercial catalyst TiO_2 (P25) without explicit change production after five cycles (Figure 10b).

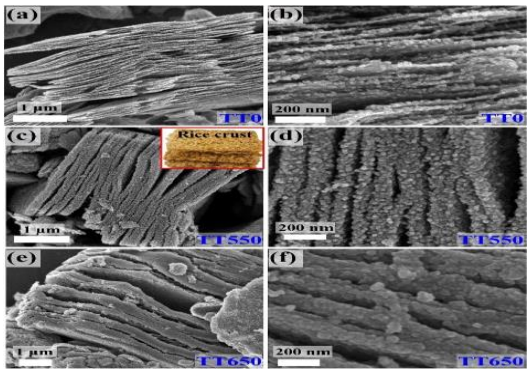

Figure 9 Field emission scanning electron microscope images of (a, b) TT0, (C,D) TT550 and (e,f) TT650. Adapted with a copyright permission from ElSEVIER 2018 [41] .

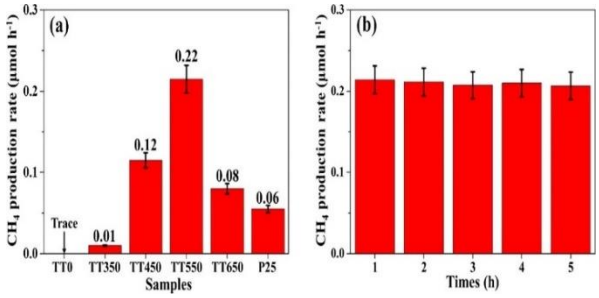

Figure. 10 (a) Comparison of the photocatalytic CO_2 reduction performance of the prepared samples and P25 for CH_4 production. (b) Photocatalytic CO_2 reduction stability test of TT550. Adapted with copyright permission from Elsevier 2018 [41].

2.3.1.4 MXeneSingle-Atom Catalyst.

A novel of facile fabrication of Single-atom catalyst by means of self-reduction stabilization process at ambient temperature using Ti_3C_2, revealing Ti defects and its

susceptibility for reduction [42]. An in situ etching for the MAX phase using LIF and HCL was used to selectively etch the Al layer Scheme 11. Resulting in MXene characterized by surface functional groups (-O2-, -OH-, and -F-) that acts as an active surface site for adsorption of metal precursors and hence, have a higher tendency for consecutive reduction and anchoring of single metal atoms. However, throughout the process, it was noticed that some Ti atoms were also ripped off despite the moderate conditions, resulting in Ti-defect. Such a defect is considered to be an additional surface-active site to host and stabilize single metal atoms where the concentration of vacancies highly depended on the concentration of HF. As an example, Pt was slowly added dropwise to MXene while stirring, and then the reaction was left for 8 hours. The formed MX-Pt was then precipitated and centrifuged by acetone. During the reaction, Pt^{4+} ions from $[PtCl_6]^{2-}$ were slowly reduced by the unstable and reductive Ti vacancies occupying the Ti-defects. Hence a strong Pt-C bond is formed, resulting in a stabilized MX-Pt. As a result, this facile fabrication method of simultaneous adsorption and reduction of SAC provides a simple alternative route rather than the multistep calcination process. Uniform adsorption of Pt on the surface of MXene represented by the bright dots. The Pt atoms appear to be located at lattice points of Ti, which indicates that substitutional doping took place. Additionally, STEM and element mapping further confirms a uniform dispersion of Pt single atoms on MXene nanosheet. The catalytic reaction was carried out by adding DMF (2 mL), aniline (0.25 mmol), triethylhydrosilane (Et3SiH) (1.7 mmol) along with CO_2 into standard Schlenk tube along with the catalyst (0.4 mmol % of Pt with respect to aniline). The catalytic performance of the as-prepared sample resulted in a complete conversion for the N-formylation of aniline with 100 % selectivity for Formanilide with fine recyclability. Whereas pristine MXene and H_2PtCl_6 almost exhibit no products (figure12). For

comparison, Pt NPs incorporated with MXene (Pt-NPs/MX) (Pt loading is 4 wt%) were prepared and tested under the same conditions. Only an 18% conversion of CO_2 was exhibited by Pt-NPs/MX. And with a lower conversion (13%) using a commercial catalyst (Pt-NPs/C). Furthermore, it's worth noting that the concentration of Ti-defects didn't play a rule in enhancing the conversion performance of aniline. Several samples of MXene and SAC Pt/MXene were prepared with different vacancies by changing LiF concentration in order to examine their catalytic conversion performance. Again, the pristine MXene with different vacancy concentration displays negligible traces. On the other hand, all the samples of Pt anchored on MXene nanosheets display almost the same conversion as each other. Hence, the sole rule of the vacancy defects in MXene is to stabilize SAC. Compared with other reports, Pt/MXene shows magnificent performance in terms of conversion and selectivity, especially under mild conditions. DFT calculations suggest a reaction route for N-formylation of aniline using CO_2 as follows: hydrosilylation reaction (I−II), CO_2 insertion (III-TS1-IV), aniline reaction (V-TS2-VI), and reduction elimination (TS3−VII). The energy profile of the suggested pathway of the reaction illustrates a higher energy barrier for Pt NPs than SAC Pt, which serves in the superiority of catalytic performance for SAC Pt. In summary, the unparalleled features such as reduction ability of surface functional groups and Ti defects make MXene a worth candidate to support and stabilize noble SACs (ex: Ru, Ir, Rh& Pd) and non-noble metals (ex: Fe, Co& Ni) through this robust fabrication route.

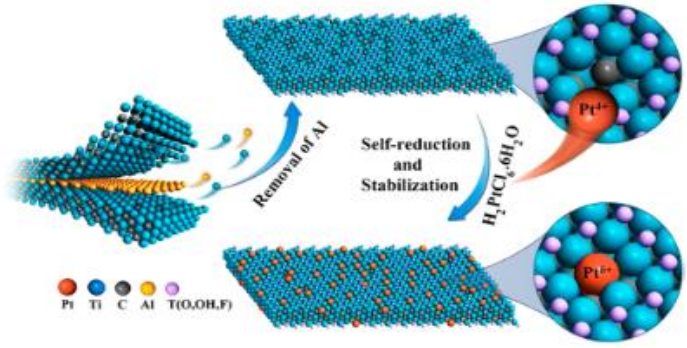

Figure 11 Illustration the simultaneous self-reduction- stabilization process for the preparation of $Pt_1/Ti_{3-x}C_2T_y$. Adapted with copyright permission from the 2019 American Chemical Society [42].

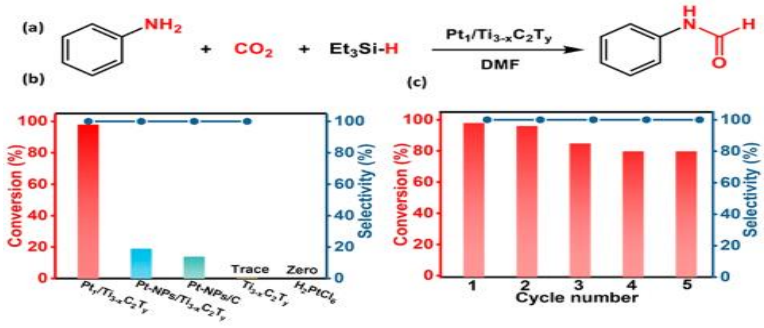

Figure 12 (a) the chemical equation for the N-formylation of Aniline with CO_2 and Et_3SiH. (b) Catalytic performance of the N-formylation of Aniline using different catalysts. (c) Recycling test of $Pt_1/Ti_{3-x}C_2Ty$ for the catalytic N-formylation of Aniline. Adapted with copyright permission from the 2019 American Chemical Society [42].

2.3.2 **N-Doped Porous Carbon Catalysis/ Gas Conversion Reactions**.

The fabrication of nitrogen-enriched carbon-based materials (denoted as 1D CNs-M) with and without metal-based catalysts is rarely reported. Meanwhile, their CO oxidation performance also is not emphasized enough compared to other applications. In this regard, recently Eid et al. have developed a simple method for controlled synthesis of 1D CNs-M nanofibers co-doped with Pd and Cu (Pd/Cu/CNNFs) through the polymerization of melamine in an aqueous solution of ethanol in the presence of Pd and Cu-precursors using nitric acid, followed by carbonization. [43]

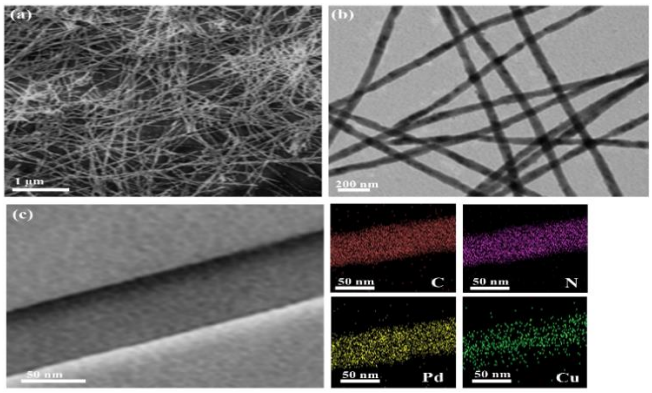

Figure 13 (a) SEM image, (b) TEM image, and (C) High-angle annular dark-field scanning transmission electron microscopy (HAADF-STEM) with the element mapping of Pd/Cu/gC_3N_4NFs. Adapted with copyright permission from MDPI 2018. [43].

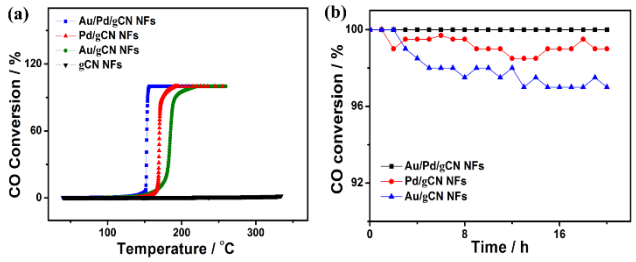

Figure 14 (a) CO conversion and (b) CO conversion durability tests measured on Pd/Cu/gC_3N_4 NFs relative to Pd/gC_3N_4 NFs, Cu/gC_3N_4NFs, and metal-free gC_3N_4NFs. Adapted with copyright permission from MDPI 2018. [43].

The obtained CNs-M formed in a high yield of 1D nanowire shape with an average length of 2 µm and 80 nm width, as shown by the SEM and TEM images (Figure 13a-c). Both Pd and Cu were uniformly distributed inside the CNs structure with an atomic connect of (1.2 wt.) as reflected in the element mapping (Figure 13d). The nanowires possess a high surface area of (120 m2 g-1), which was slightly higher than that of metal-free CNs nanowires. The CO oxidation activity and stability of Pd/Cu/CN NFs were significantly higher than that of Pd/CN NFs, Cu/CN NFs, and metal-free CN NFs. In particular, Pd/Cu/CN NFs achieved a complete CO conversion at 149 °C, that was more active than that of Pd/CN NFs (283 °C), and Cu/CN NFs (329 °C) whereas CNs NFs could not oxidize CO even after continuous heating till 400 ^{o}C (Figure 14a). Moreover, Pd/Cu/CN NFs remained active without any significant loss after 20 h of accelerated stability testes (Figure 14b). This is originated from coupling the impressive physical and chemical properties of CNs NFs with the outstanding catalytic merits of Pd and Cu. In addition, Eid et al. have tailored the fabrication of porous gC_3N_4 nanotubes codoped with Au and Pd (Au/Pd/gC_3N_4NTs) at the atomic level based on the polymerization of melamine in glycol-mediated solution contains Au- and Pd precursors followed by annealing under nitrogen. [44]

The SEM and TEM images revealed the high mass formation of uniform Au/Pd/gC_3N_4NTs nanotube morphology with an average longitude of 1.3 µm and width of 95 nm (Figure 15a-b) The HAADF-STEM showed the 1D porous nanotube morphology with a well-defined porous interior and smooth surface (Figure 15c). The element mapping analysis clearly displayed the presence of C, N, Au, and Pd with atomic ratios of 40, 59, 0.52, and 0.48, respectively (Figure 15d-g). The high surface area of the obtained Au/Pd/gC_3N_4NTs reached as much high as (320.6 m^2 g^{-1})

calculated using the density functional theory from the nitrogen adsorption-desorption data. [44]

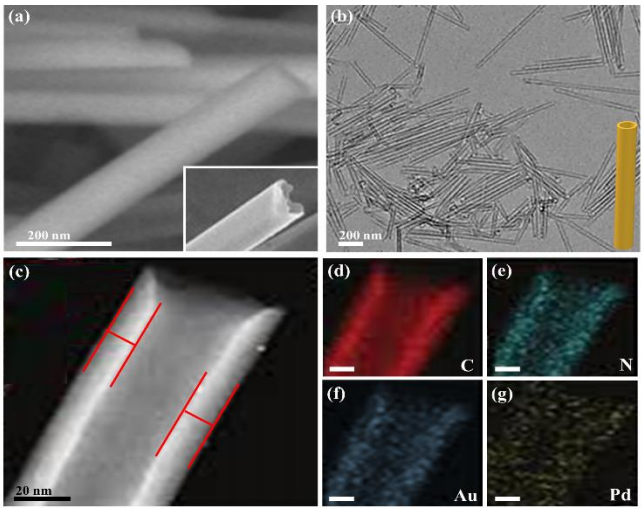

Figure 15 (a) SEM image, (b) TEM image, (c) HAADF-STEM, and (d-g) element mapping analysis of AuPd/gC_3N_4NTs. Adapted with a copyright permission from 2019 American Chemical Society [44] .

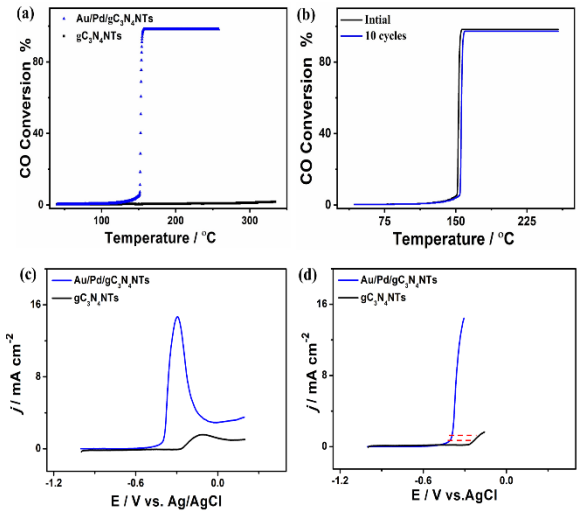

Figure 16 (a) CO conversion and (b) CO conversion durability. (c) Cyclic voltammogram and (d) measured in CO-saturated 0.1 M KOH at 50 mVs^{-1} . Adapted with copyright permission from 2019 American Chemical Society [44].

The designed Au/Pd/gC_3N_4NTs showed a significantly higher CO conversion efficiency and durability than that of metal-free gC_3N_4NTs. Particularly,

Au/Pd/gC_3N_4NTs were able to achieve a full CO conversion at 165 ^oC, whereas at 300 ^oC the metal-free gC_3N_4NTs did not show any noticed activity towards CO conversion (Figure 14a). This is in addition to the greater stability of Au/Pd/gC_3N_4NTs, which kept their catalytic activity without any significant loss after 10 durability cycles (Figure 16b). This was furthered evidenced in the electrocatalytic measurements. The CVs demonstrated the superior ability of Au/Pd/gC_3N_4NTs to adsorb a higher amount of CO under lower potential than that on gC_3N_4NTs (Figure 16c). In addition, the CO oxidation kinetics on Au/Pd/gC_3N_4NTs was quicker than that on gC_3N_4NTs under an applied potential, as indicated by the dashed lines in (Figure16d).

Another interesting example is the controlled synthesis of porous graphitic gC_3N_4 nanotubes doped with Pd and Cu (denoted as PdCu/gC3N4NTs) at the atomic level based on the polymerization of melamine in an aqueous solution of ethylene glycol containing metal salts followed by annealing at 550 ^oC under nitrogen.[26] The as-formed PdCu/gC3N4NTs showed a significant electrochemical and photoelectrochemical CO_2 reduction activity and durability compared to metal-free gC_3N4NTs. In particular, the obtained CO_2 reduction current on Pd/Cu/gC_3N_4NTs was about 5.5 fold greater than that of gC_3N_4NTs under the same applied potential (Figure 17a). The superior performance of Pd/Cu/gC_3N_4NTs is due to their greater conductivity and fast charge transfer, as evidenced in the electrochemical impedance spectroscopy (EIS). The UV-light irradiation enhanced the CO_2 reduction efficiency by 3.5 times than under dark (Figure 17 b). The GC-FID reflected that the main CO2 reduction product was formic acid with an inferior amount of methanol (Figure 17c). The TEM images showed that Pd/Cu/gC_3N_4NTs reserved their porous nanotube structure without any significant changes after the accelerated durability cycles for CO2 reduction testes (Figure 17d-e).

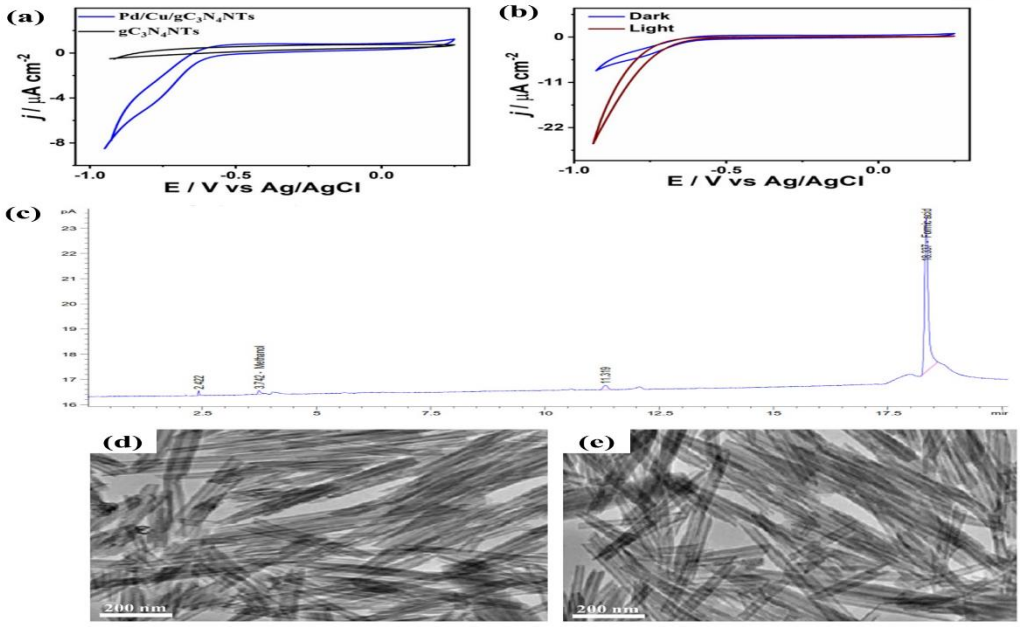

Figure 17 (a) CVs measured in an aqueous solution of 0.5 M $NaHCO_3$ saturated with CO2 under dark at room temperature and at a scan rate of 50 mVs-1. (b) CVs tested in 0.5 M $NaHCO_3$ saturated with CO2 under dark compared to light at room temperature and at a scan rate of 50 mVs-1. (c) GC-FID for CO2 product obtained using the PerkinElmer Elite-624 column at 35 °C. TEM image of Pd/Cu/gC_3N_4NTs before (d) and after (e) CO2 reduction. Adapted with copyright permission from ELESVIER2019 [26].

Chapter 3: Experimental

3.1 Material

3.11 MXene-based

Aluminum titanium carbide powder MAX-phase ((Ti_3AlC_2), 98 %) was purchased from Carbon-Ukraine Ltd), and Dimethyl sulfoxide (DMSO), (C_2H_6OS, 99.7%) will be obtained from Fisher Scientific International, Inc. Hydrofluoric acid (HF, 48%) was obtained from VWR Chemicals BDH. Sodium hydroxide (NaOH, 99.9 %), and zinc chloride (99%), and Copper(II) chloride (99 %) were ordered from Sigma Aldrich (Munich, Germany).

3.12 Carbon capsule materials.

Tetraethyl orthosilicate (TEOS), absolute ethanol, 35 wt.% ammonia solution, melamine, resorcinol, 36% formaldehyde, 65% hydrofluoric acid were obtained from Sigma Aldrich Chemie GmbH (Munich, Germany). Zinc oxide nanoparticles (ZnO) with average size > 50 nm was Purchased from Alfa Aesar. All the chemicals were of analytical grade and used as received without further purification.

3.2 Synthesis

3.2.1 Synthesis of Cu-Zn/$Ti_3C_2T_x$ nanosheets

In the typical synthesis, 10 mL of the $Ti_3C_2T_x$ MXene suspension was dispersed in 100 ml of deionized water. Then sonicated for 1 hr to obtain a transparent $Ti_3C_2T_x$ solution (1mg/mL). Zn and Cu metal solutions were prepared separately by adding 100µL from a $ZnCl_2$ (1mg/mL) and $CuCl_2.2H_2O$ (1 mg/mL) solutions, respectively, into two separate 10mL of deionized water. Then, an aqueous solution of $CuCl_2$ (0.5 wt. %) and $ZnCl_2$ (0.5 wt. %) were dropwise intervals to the as-prepared $Ti_3C_2T_x$ solution under agitated stirring at room temperature for 24 h. After that, the final product of Cu-

$Zn/Ti_3C_2T_x$ nanosheets was purified via consecutive centrifugation and washing cycles at 7000 rpm with acetone and then dried under vacuum-dried overnight at 50 °C.

3.2.2 Synthesis of Spherical Mesoporous Carbon doped with ZnO.

Firstly, (3.0 gm) of ZnO nanoparticles were dispersed in 380 ml of Ethanol. Then, 35 wt. % ammonia solution was added dropwise to the solution at room temperature to make the stock solution with pH ranging from 10 to 11.4. Subsequently, TEOS (11.0 ml) was added to the catalyst solution at one time, and then the resultant TEOS-ethanol biphasic system was stirred at 100 C for 24 h in a water bath. The magnetic stirring rate was kept at ca. 500 rpm using a 2 cm long Teflon-coated stirring bar. A homogeneous, optically white color of spherical silica was obtained.

Secondly, (2.50 gm) of resorcinol and (1.0 gm) Melamine were dissolved individually in 5 ml of deionized then added to the stock solution and continue stirring for 1h. after that, (0.5 ml) Formaldehyde was drop wisely added to the solution and of raising the temperature to 150 ℃ for another 24 h.

Finally, the as-formed precipitate was washed with ethanol and dried at 120 °C for 12 h prior to annealing at 650 °C (3° / min) for 2 h. under Argon after cooling to the room temperature, the carbonized material was etched using 10% HF for 24h then washing with deionized water, dried and the obtained final product was kept for further characterization.

3.3 Characterization

3.3.1 X-ray Photoelectron Spectroscopy (XPS)

The electronic configuration and the surface composition were investigated by X-ray photoelectron spectroscopy (XPS), Model Axis (Ultra DLD XPS Kratos, Manchester, UK) and equipped with a monochromatic Al Kα radiation source (1486.6 eV) X-ray Power, 15 kV, 20 mA under a UHV environment (ca. 5x10-9 Torr). XPS is equipped with a set of chambers to transfer sensitive samples from the sample transfer chamber (STC) after maintaining a vacuum to the XPS surface analysis chamber (SAC), which is under ultra-high vacuum.

XPS spectra were obtained by irradiating MXene, Zn/Ti_3C_2T, Cu/Ti_3C_2T, and Cu-Zn/Ti_3C_2T, with a beam of X-rays while simultaneously measuring the kinetic energy and number of electrons that escape from the top 0 to 10 nm of the material being analyzed. The full survey has been done at 160 EV passing energy. (based on the use of monochromatic X-Ray Source- Al Kα source) Also, high resolution at 20 EV passing energy.

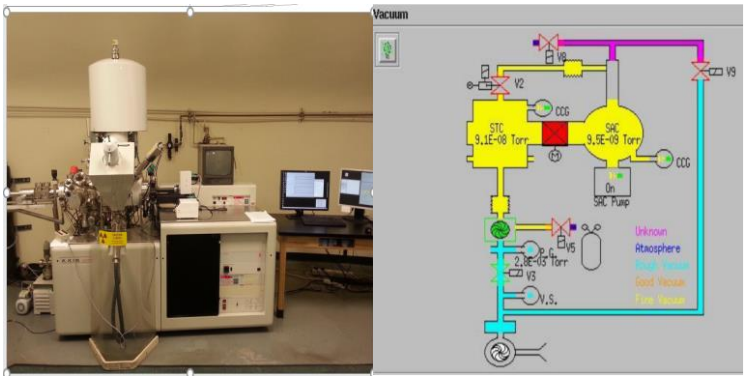

Figure 18. XPS DLD Axis Ultra

3.3.2 Transmission electron microscope (TEM)

The shape and composition of typically prepared materials were investigated using a transmission electron microscope (TEM, TecnaiG220, FEI, Hillsboro, OR, USA).

3.3.3 HPHT catalytic Reactor

Catalytic conversion of CO_2 The catalytic process was carried out via placing 100 mg of the as-formed catalysts in a fixed-bed reactor (model) connected to an online gas chromatography fig 14. The catalyst should be initially pretreated under H_2 gas (20 mL/Min) gas at 200 for 2h. Following the cooling, the catalyst was exposed to the CO_2/H_2 ratio 1/3 with a total flow of 65 mL/min at temperature 200 C and atmospheric pressure. 50 ml/min mix gas and 15 ml/min H2 pure The gas products were analyzed by the GC-TCD (Agilent, USA).

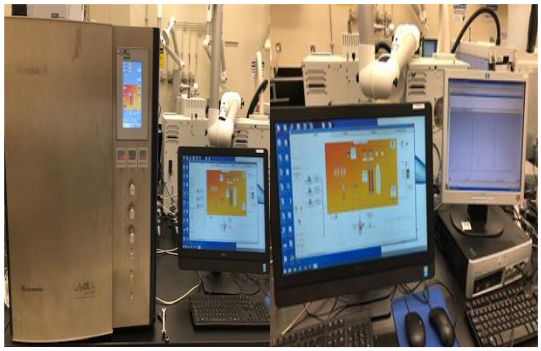

Figure 19. high pressure and temperature catalytic reactor.

3.3.4 X-Ray Diffraction (XRD)

The crystallinity and phase structure was performed using X-ray diffraction pattern (XRD) model X`Pert-Pro MPD, PANalytical Co., Almelo, Netherlands) using Cu Kα X-ray source (λ = 1.540598 Å), shown in Figure 15. the device made of three main elements, including cathodic ray tube, a sample holder, and an X-ray detector. In the cathodic ray tube, the X-rays are generated where a filament is heated to produce electrons that accelerate toward the anode by applying a high voltage of 45 kV. When the electrons gain enough energy to hit the inner shell of the target material, an X-ray of 1.54 nm wavelength is produced. In the holder section, a divergent slit of 0.19 mm focusses the X-ray on the sample to ensure more area of the sample is exposed to get the intensity of the scattered ray. This intensity is measured by the rotation detector.

Also, the aligned geometry rotation at an angle of 2θ is maintained by the goniometer at the center of the device.

Figure 20.The PAN analytical X-Ray diffractometer

3.3.5 Scanning Electron Microscopy (SEM)

The as-prepared materials were imaged using a High field emission scanning electron microscopy HFESEM (FEI NOVA NANOSEM 450, Hillsboro, OR, USA) attached to an energy dispersion X-ray analysis unit EDX shown in (Figure 20) was used to study the morphology of MXene, Zn/Ti_3C_2T, Cu/Ti_3C_2T and Cu-Zn/Ti_3C_2T at different magnitude 2000, 5000, and 10,000x. To get high-resolution images, the samples were placed in a distance between the sample and the source of electrons of 10 nm. The machine was operated at a high voltage of 12.5 kV. Then, the electrons were transferred via high-speed beams and hit the sample. The reflected electrons were detected by SEM, and the absorbed ones interact with the specimen to provide a semi-quantitative elemental analysis by EDX.

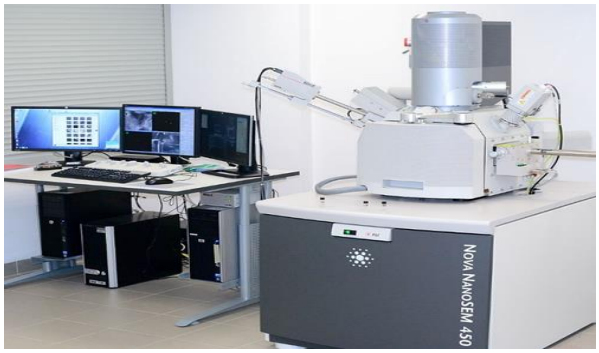

Figure 21. High Field Emission Scanning Electron Microscope

3.3.6 Electrochemical Setup for CO_2 Reduction

The electrochemical measurements were performed on a Gamry electrochemical analyzer (reference 3000, Gamry Co., USA), using a three-electrode cell involving a Pt wire, Ag/AgCl, and glassy carbon (GC, 5 mm) as a counter, reference and working electrode, respectively. The GC electrodes were covered with 15 μg cm^{-2} of each catalyst, followed by the addition of 5 μL Nafion (0.05%) and left to completely dry before the measurements. The cyclic voltammograms (CVs) cleaning was performed in an N_2-saturated aqueous solution of 0.5M $NaHCO_3$ at a sweeping rate of 200 mVs^{-1} at room temperature. The CVs were cycled in CO_2-saturated 0.5 M NaHCO3 at 50 mVs^{-1}. The ICP was used to determine the amount of each catalyst on the electrode surface.

Figure 22. Potentiostat instrument, Model: GAMRY “Reference 3000.”

Figure 23. UV Simulator Instrument, glassy electrodes.

3.3.7 Ultra-Performance Liquid Chromatography (UPLC)

Formic acid has been quantified by using Water Acquity UPLC with UV, and PDA detector at 210 nm and the column used for separation was Agilent C18 4 um particle size, 4.6 x 150mm dimensions at ambient temperature. Isocratic elution used at constant flow rate 1 ml/min of sulfate buffer (1 mmol/L H_2SO_4+ 8 mmol/L Na_2SO_4(pH 2.8)).

Figure 24 Water Acquity UPLC with UV and PDA detector

3.3.9 Gas Chromatograph analysis –TCD

Outlet gas product from the HPHT reactor was injected Online to the GC-TCD gas valve by using the following parameters. Oven 32^{o}C hold 3 min then heating till 150 ^{o}C with rate 30 c/min. injector 150 ^{o}C and detector 200 ^{o}C and calibrated by standard composition.

Figure 25 shows Agilent Gas Chromatograph with a TCD detector.

3.3.8 Thermogravimetric analysis (TGA)

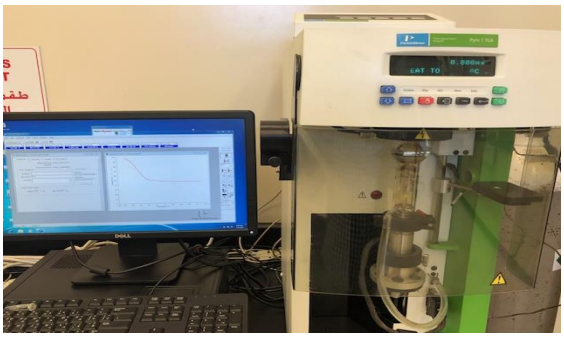

Figure 26 Shows The Perkin Elmer TGA, Pyris 1 model.

The Perkin Elmer TGA, Pyris 1 model – was used for the thermogravimetric analysis of carbon-based catalyst samples. The temperature operating range of the equipment is 30ºC to 900 Cº and calibrated at different temperature rates. 1.5 mg of the material was introduced in a pan and placed onto a hang-down wire suspended from a microbalance down into the furnace. The experiment was performed at a heating rate of 5 ºC/min, starting from 30 to 800 ºC.

3.3.10 Physisorption analysis (BET)

Around 0.2 grams of sample is weighed and poured into the holder of micromeritics device. Then, the sample degassed at 150C under vacuum pump of 10-4 bar for 24 h in order to remove all residues inside the matrix of sample and to be ready to measure BET

Figure 27 shows Micromeritics BET physisorption for surface area test.

Chapter 4: Results and Discussion

4.1 Electrochemical and Photoelectrochemical. (Part#1)

The SEM analyses were carried out to confirm the shape and composition of the images of the materials. Figure 28a-b shows the SEM images of Max (Ti_3AlC_2) phase different magnifications, which depicted the typical stacked multilayered sheets-like structure. The sheets are highly compacted with an average diameter of 5 µm. The EDX analysis revealed the presence of Ti, Al, C, and O with atomic contents of 25.42, 6.24, 45.91, and 11.44, respectively (Figure 28c).

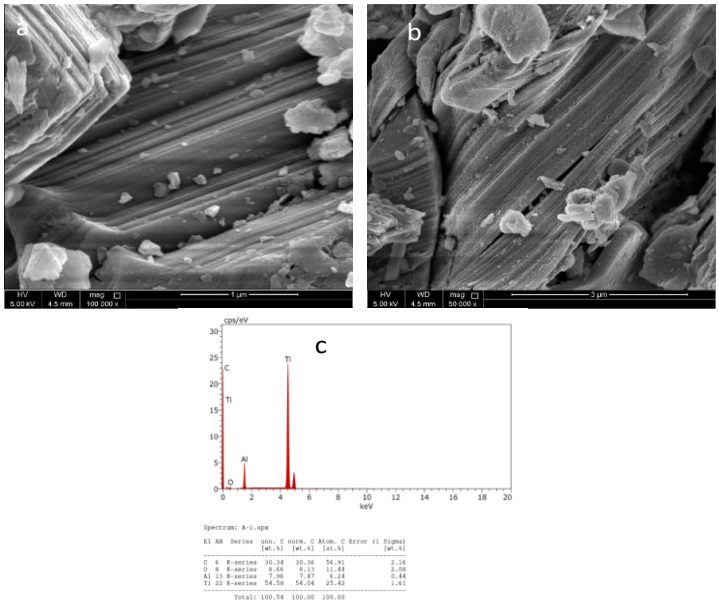

Figure 28 (a ,b &c) Shows the SEM images and EDX of Ti_3AlC_2 Max phase.

The Max phase was etched chemically using HF solution as mentioned above in the excremental sections to form MXene followed by intercalation with DMSO and delamination under ultrasonic treatment to produce Ti_3C_2T MXene (Figure 29). The obtained nanosheets are highly exfoliated with an average interlayer spacing of 100 nm (Figure 29a-c), which clearly displayed the successful selective etching of Al by HF. This is furthered proved by the EDX, which showed the atomic of 16.05 for Ti, 63.14 for C, and 17.13 for O (Figure 29d) as well as some inferior amount of un-etched Al and F.

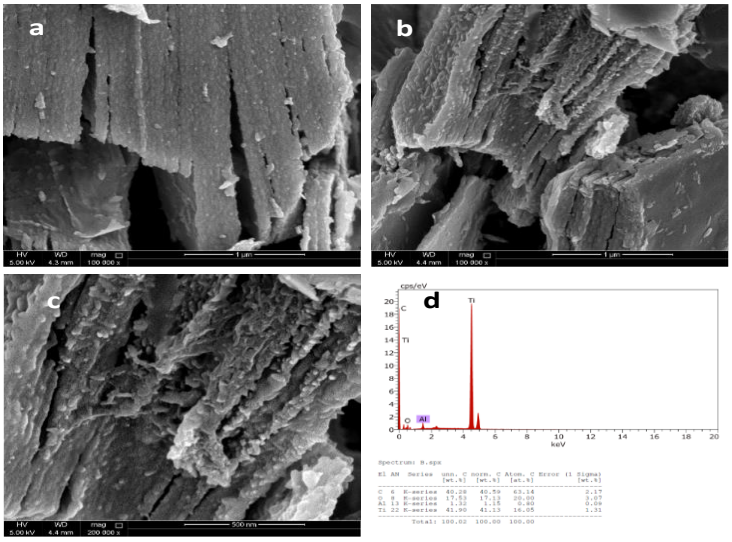

Figure 29 (a, b, c &d). shows the SEM images and EDX analysis of Ti_3C_2T MXene.

The as-obtained Ti_3C_2T was doped with Cu atomically to form Cu/Ti_3C_2T. The SEM images reflected that the sheets were more exfoliated, and the interlayer spacing increased significantly, indicated the doping effect (Figure 30a-c). Also, the sheets became thinner after doping. The EDX proved the presence of Cu, Ti, C, and O with atomic ratios of 0.18, 20.87, 56.73, 22.22, respectively (Figure 31d).

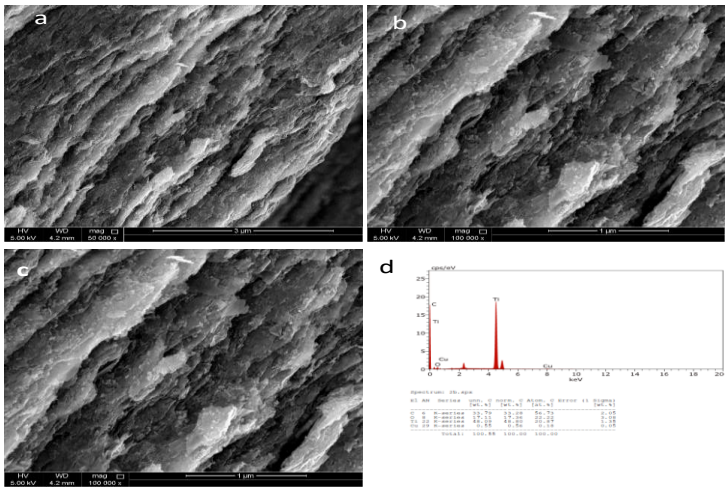

Figure 30 (a , b, c &d). shows the SEM images and EDX analysis of the as-synthesized materials after doped with Cu atoms.

The as-obtained Ti_3C_2T was doped with Zn atomically to form Zn/Ti_3C_2T. The SEM images reflected the formation of thin and crumbed sheets with a bigger interlayer spacing due to the co-doping effect with both Zn and Cu (Figure 31a-c). The EDX proved the presence of Cu, Zn, Ti, and C with atomic ratios of 0.1, 19.32, 61.38, and 17.54, correspondingly (Figure 31d).

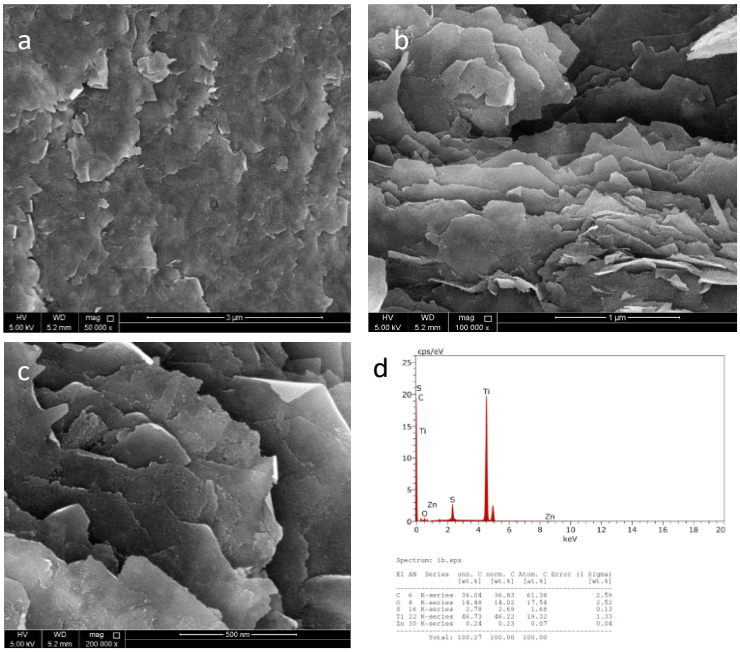

Figure 31 (a, b, c &d) Shows the SEM images and EDX analysis of the as-synthesized materials after doped with Zn atoms.

The as-obtained Ti_3C_2T was doped with Cu and Zn atomically to form $Cu/Zn/Ti_3C_2T$. The SEM images reflected that the sheets became more exfoliated, the interlayer spacing increased, and sheets- thicknesses decreased significantly compared to Cu/Ti_3C_2T (Figure 32a-c). The edges of the sheets showed some crumbing shape after Zn doping. The EDX proved the presence of Cu, Zn, Ti, and C with atomic ratios of 0.14, 0.1, 16.55, 61.38, and 21.09 (Figure 32d).

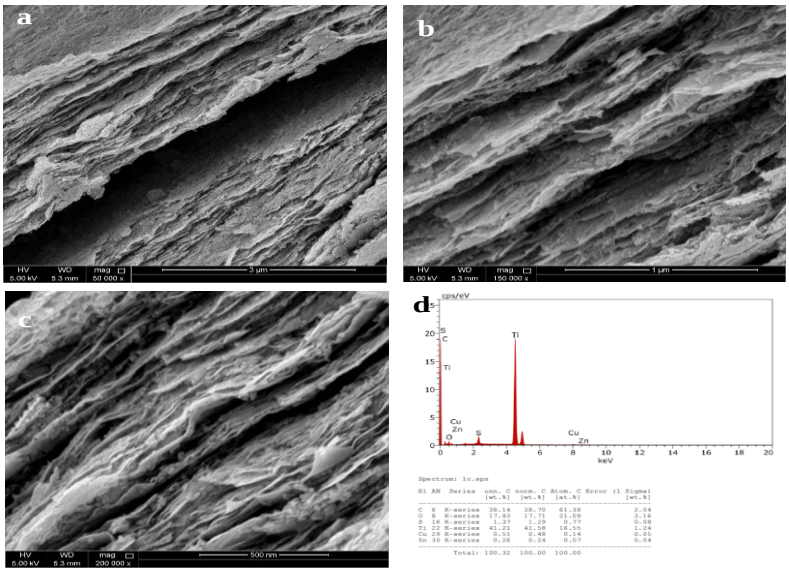

Figure 32 shows the SEM images and EDX analysis of the as-synthesized materials after doped with Cu/Zn atoms.

The elemental mapping analysis was hired to confirm the composition of thus obtained Cu/Zn/Ti_3C_2T (Figure 33a-d), which demonstrated the homogenous distribution of Cu, Zn, Ti, and C. This further revealed the successful co-doping with both Cu and Zn.

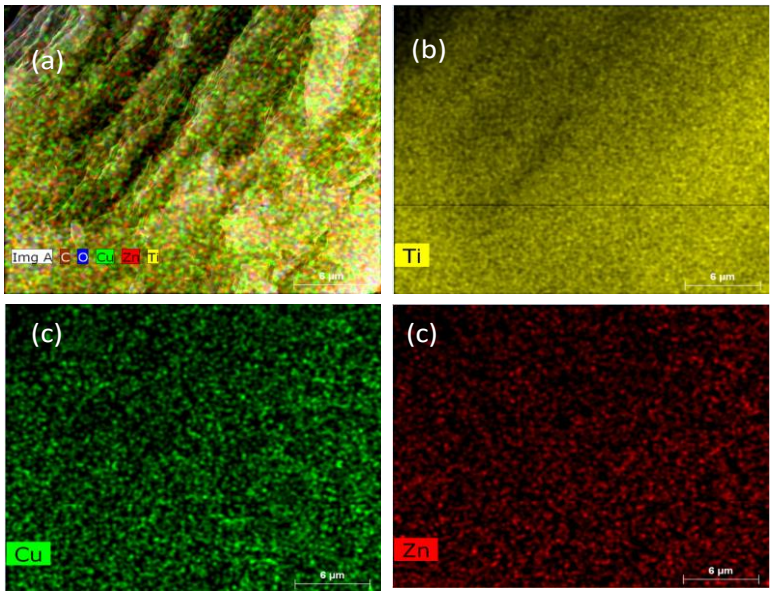

Figure 33 Elemental mapping of the as-synthesized materials after doped with Cu/Zn atoms.

The TEM analysis was carried out to get more insights into the morphology and composition of thus formed Cu/Zn/Ti_3C_2T.

The TEM images showed the formation of 2D nanosheets with average dimensions of 200 nm in length and 100 nm in width (Figure 34a). The nanosheets were thin with crumbed edges, as evidenced by the high magnification TEM image (Figure 34b). The TEM could not reflect the presence of both Cu and Zn due to their doping at the atomic level in line with elsewhere reports. [45-49] .

The HAADF-STEM image also confirmed the crumbed and 2D shape of thus formed Cu/Zn/Ti_3C_2T nanosheet (Figure 35a). The elemental mapping analysis clearly warranted the coherent distribution of Cu, Zn, Ti, C, and F (Figure 35 b-g) demonstrated the successful co-doping with both Cu and Zn in line with the EDX analysis (Figure 35h).

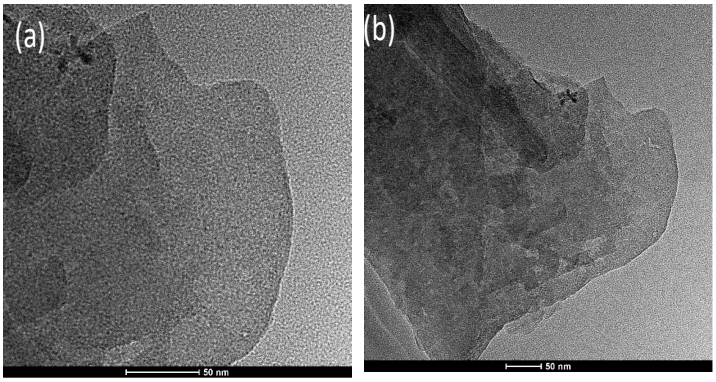

Figure 34 Shows the TEM analysis of Ti_3C_2 T MXene and as-synthesized materials after doped with Cu/Zn atoms.

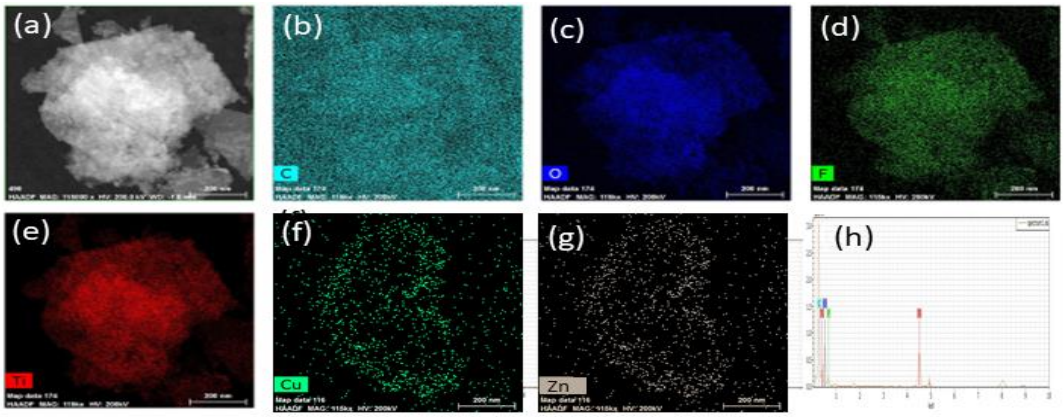

Figure 35 (a) HAADF-STEM image of MXene-Cu/Zn and its elemental mapping analysis (b) for C, (c) for O,(d) for F, (e) for Ti. (f) EDX analysis.

Figure 36 showed the XRD analysis of the as-synthesized Cu/Zn/Ti_3C_2T compared to Cu/Ti_3C_2T, Zn/Ti_3C_2T, and metal-free Ti_3C_2T. All materials displayed the only typical XRD diffraction patterns of Ti_3C_2T with the main facet of {002} of TiC at 7^o in line with ICDD:98-061-8950. There are not any kind of peaks that were resolved for both Cu and Zn, indicated their atomic doping inside Ti_3C_2T in agreement with elsewhere reports on the metal dopants at the atomic level. [45-50] However, the doping effect could be seen in the substantial negative shift to lower 2θ angle value of {002} facet as well as the decrease in the intensities and broaden of the XRD diffraction patterns.[48-50]

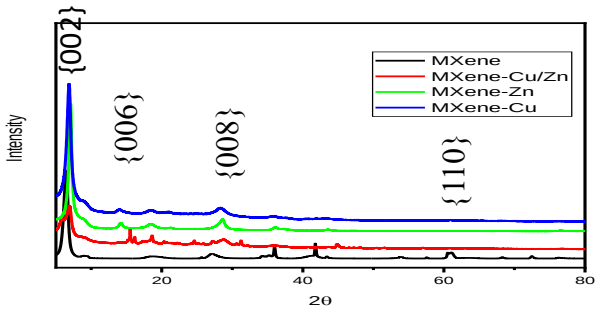

Figure 36 displays the XRD spectra of MXene, Zn/Ti_3C_2T, Cu/Ti_3C_2T, and Cu-Zn/Ti3C2T.

Figure 37 shows the XPS full survey of the pure MAX-phase, which showed the spectra of Ti, C, Al, O, and F with atomic ratios of 11.19, 34.43, 12.47, 39.79,0 and 2.12 respectively. The detailed composition of the MAX phase and the position of each spectrum are shown in (Table 2).

Compared to Pure MAX-phase, the as-formed Ti_3C_3T clearly demonstrated the presence of the valence states of Ti 2p, C1s, Al 2p, O 1s, F1s, and N1s (Figure 38). The surface compositions revealed that the atomic content of Ti, C, Al, O, and F are about 12.31, 44.61, 0, 27.94, and 13.30, respectively, indicated the formation of MXene without detection of any spectrum for Al or any other impurities. The detailed composition of the Ti_3C_2T and the position of each spectrum are shown in Table 2.

The high-resolution XPS spectra of Ti 2p in MXene sample were de-convoluted into 6 peaks at 2 peaks located at 455.49 eV for Ti $2p_{3/2}$ and at 461.35 eV for Ti $2p_{1/2}$ assigned to Ti-C along with 4 peaks at binding energies of 457.48, 459.37, 462.99 464.93 eV for the Ti-O (Figure 39a). [51] Likewise, the spectra of C 1s revealed 4 peaks at 281.8, 285.1, 287.3, 289.1 eV attributed to C-Ti, C-C, C-O, O-C=O, respectively. (Figure 39b). The high-resolution XPS spectra of O 1s were fitted into two peaks at the binding energies of 530.6 eV for Ti-O and 532.6 eV for Ti-OH (Figure 39c). This demonstrated that the majority of Ti was in the oxide state with a ratio of 60.6/39.4 % for Ti-O/TiC, respectively. The detailed composition of each phase is shown in (Figure 39d).

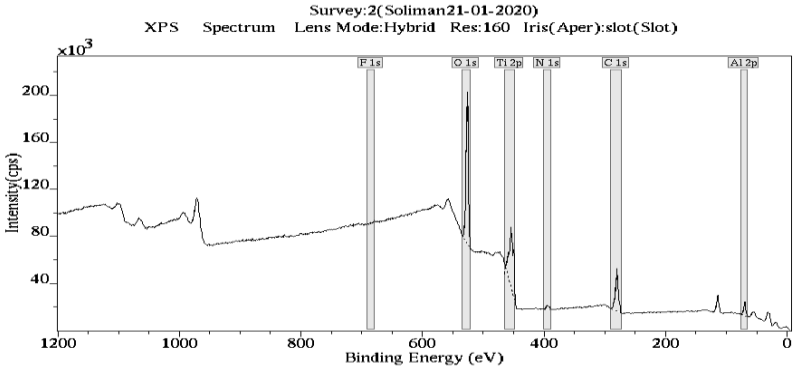

Figure 37. shows the full XPS survey of Max-phase before etching by HF

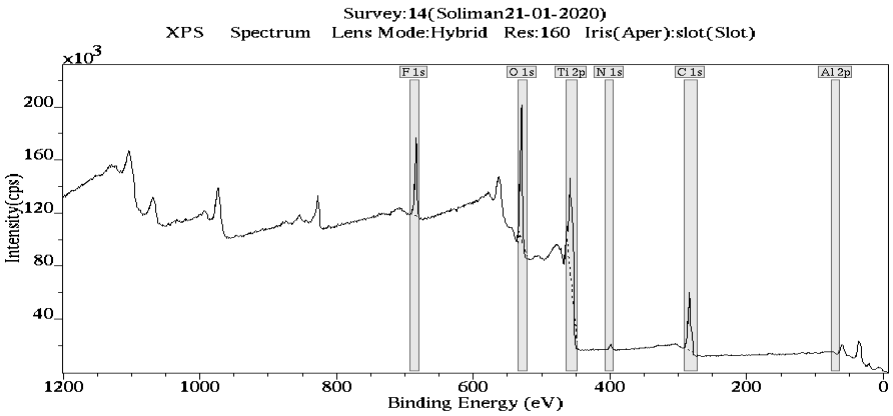

Figure 38. shows the full XPS survey of MXene and shows there is no Aluminum after etching of the Max-phase.

Quantification Report

/c:/data/Soliman21-01-2020.dset — Thu Feb 13 17:12:18 2020

State : Angle Name : Position 1

Peak	Type	Position BE (eV)	FWHM (eV)	Raw Area (cps eV)	RSF	Atomic Mass	Atomic Conc %	Mass Conc %
Ti 2p	Reg	455.000	8.013	420690.0	2.001	47.878	11.19	27.44
C 1s	Reg	281.000	3.430	174438.3	0.278	12.011	34.43	21.19
Al 2p	Reg	70.000	3.315	46745.3	0.193	26.982	12.47	17.24
O 1s	Reg	527.000	4.163	573171.7	0.780	15.999	39.79	32.62
F 1s	Reg	681.000	0.758	0.0	1.000	18.998	0.00	0.00
N 1s	Reg	396.000	6.052	19706.7	0.477	14.007	2.12	1.52

State : Angle Name : Position 2

Peak	Type	Position BE (eV)	FWHM (eV)	Raw Area (cps eV)	RSF	Atomic Mass	Atomic Conc %	Mass Conc %
Ti 2p	Reg	459.000	6.685	407473.3	2.001	47.878	12.31	31.86
C 1s	Reg	285.000	3.774	198798.3	0.278	12.011	44.61	28.95
Al 2p	Reg	2201.000	1.000	0.0	0.193	26.982	0.00	0.00
O 1s	Reg	530.000	3.575	354861.7	0.780	15.999	27.94	24.15
F 1s	Reg	685.000	3.132	211626.7	1.000	18.998	13.30	13.65
N 1s	Reg	400.000	5.718	15021.7	0.477	14.007	1.84	1.39

Table 2 shows the quantification report for the max phase and MXene on the surface.

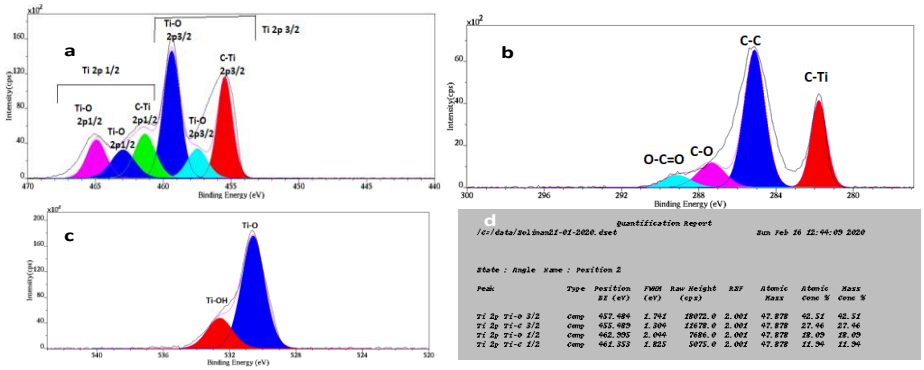

Figure 39 The high-resolution XPS spectra of Ti 2p, C1s, O1s, and Ti 2p quantification ratios in the as-formed Ti_3C_2T.

Figure 40 shows the XPS survey of the as-prepared Zn/Ti_3C_2T, which demonstrated the presence of the valence states of Ti 2p, C1s, Al 2p, O 1s, F1s, and Zn 2p. The surface compositions revealed that the atomic content of Ti, C, O, F, and Zn are about 22.16, 45.66, 20.39, 10.20, and 0.25, respectively, as shown in Table 3, indicates the successful doping of Ti_3C_2T with Zn.

The high-resolution XPS spectra of Ti 2p in the as-prepared Zn/Ti_3C_2T were de-convoluted into 6 peaks at 2 peaks located at 455.7 eV for Ti $2p_{3/2}$ and at 461.61 eV for Ti $2p_{1/2}$ assigned to Ti-C along with 4 peaks at binding energies of 457.7, 459.5, 463.2, 465.1 eV for the Ti-O (Figure 41a). Likewise, the spectra of C 1s revealed 4 peaks at 281.95,285.2, 287.1, 289.1 eV attributed to C-Ti, C-C, C-O, O-C=O, respectively. (Figure 41b). The high-resolution XPS spectra of O 1s were fitted into two peaks at the binding energies of 530.58 eV for Ti-O and 532.68 eV for Ti-OH (Figure 41c). The ratio of Ti-O/TiC was about 48.55/51.44 % (Table 4). The high-resolution of Zn2p has been fitted into 2 peaks at binding energies of 1022 eV due to Zn $2p_{3/2}$ and 1044.52 eV due to Zn $2p_{½}$, demonstrated the presence of Zn in the metallic state (Figure 41 d). The noticed peak at 1036.3 eV may be due to Zn bonded to Ti [52].

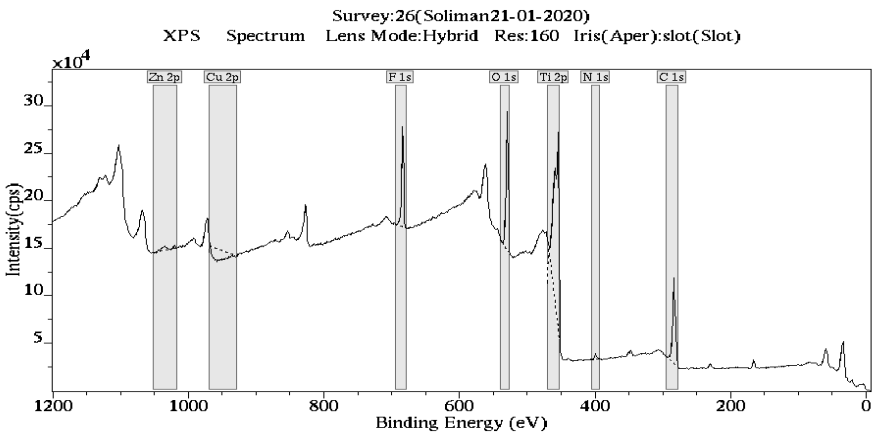

Figure 40. shows the full XPS survey of Ti_3C_2T doped with Zn

Quantification Report

/c:/data/Soliman21-01-2020.dset — Thu Feb 13 17:19:02 2020

State : Angle Name : Position 3

Peak	Type	Position BE (eV)	FWHM (eV)	Raw Area (cps eV)	RSF	Atomic Mass	Atomic Conc %	Mass Conc %
Ti 2p	Reg	456.000	8.495	1634670.0	2.001	47.878	22.16	49.02
C 1s	Reg	285.000	4.943	453006.7	0.278	12.011	45.66	25.33
O 1s	Reg	530.000	3.677	576766.7	0.780	15.999	20.39	15.07
F 1s	Reg	685.000	3.031	361400.0	1.000	18.998	10.20	8.95
Cu 2p	Reg	1201.000	1.000	0.0	5.321	63.549	0.00	0.00
Zn 2p	Reg	1036.000	8.562	47033.3	5.589	65.387	0.25	0.77
N 1s	Reg	400.000	3.159	24070.0	0.477	14.007	1.32	0.86

Table 3 shows the Quantification report of Ti_3C_2T doped with Zn on the surface.

Quantification Report

/c:/data/Soliman21-01-2020.dset — Sun Feb 16 12:44:27 2020

State : Angle Name : Position 3

Peak	Type	Position BE (eV)	FWHM (eV)	Raw Height (cps)	RSF	Atomic Mass	Atomic Conc %	Mass Conc %
Ti 2p Ti-C 3/2	Comp	455.700	1.265	33642.0	2.001	47.878	35.79	35.79
Ti 2p Ti-O 1/2	Comp	463.220	1.306	34358.0	2.001	47.878	36.58	36.58
Ti 2p Ti-O 3/2	Comp	457.699	1.783	11247.0	2.001	47.878	11.97	11.97
Ti 2p Ti-C 1/2	Comp	461.610	1.998	14703.0	2.001	47.878	15.66	15.66

Table 4 shows the quantification report Ti 2p ratios in the as-prepared Zn/Ti_3C_2T

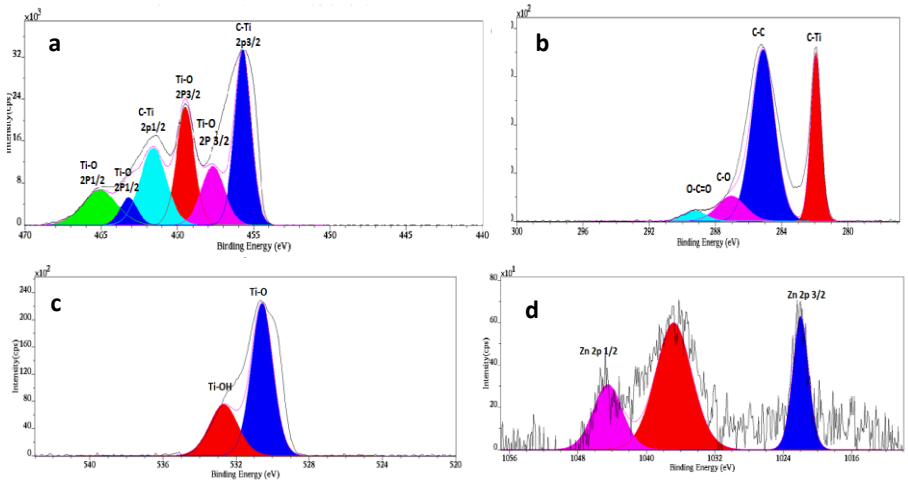

Figure 41 (a, b, c &d) The high-resolution XPS spectra of Ti 2p, C1s, O1s, and Zn 2p in the as-prepared Zn/Ti_3C_2T.

Figure 42 shows the XPS full survey of the as-synthesized Cu /Ti_3C_2T, which clearly demonstrated the presence of the valence states of Ti 2p, C1s, O 1s, F1s, and N1s as well as Cu 2p. The surface compositions revealed that the atomic content of Ti, C, O, F, and Cu are about 22.65, 41.34, 24.55, 9.51, and 0.09, respectively, as shown in Table 5. This indicates the successful doping of Ti_3C_2T with Cu.

The high-resolution XPS spectra of Ti 2p in the Cu /Ti_3C_2T sample were de-convoluted into 6 peaks at 2 peaks located at 455.5 eV for Ti $2p_{3/2}$ and at 461.5 eV for Ti $2p_{1/2}$ assigned to Ti-C along with 4 peaks at binding energies of 457.48, 459.4, 463.2, 464.9 eV for the Ti-O (Figure 43a). Likewise, the spectra of C 1s revealed 4 peaks at 281.9, 285.1, 286.7, 289.2 eV attributed to C-Ti, C-C, C-O, O-C=O, correspondingly. (Figure 43b). The high-resolution XPS spectra of O 1s were fitted into two peaks at the binding energies of 530.5 eV for Ti-O and 532.7 eV for Ti-OH (Figure 43c). The ratio of Ti-O/TiC was about 53.86/46.14 % (Table 6). The high resolution of Cu2p has been fitted with two main peaks at binding energies 932.3 e for Cu $2p_{3/2}$ and 952.15 eV for Cu $2p_{1/2}$ (Figure 43d), indicated the successful doping with Cu (Figure 43d).

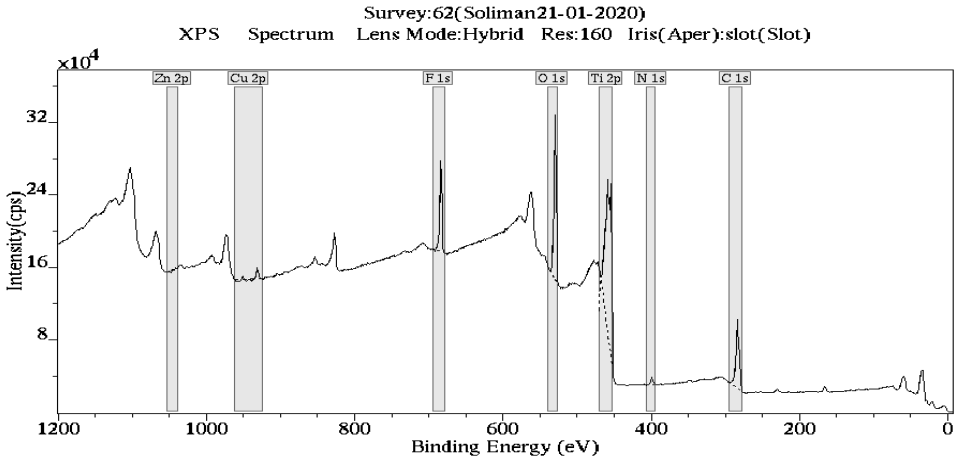

Figure 42. shows the full XPS survey of Ti_3C_2T doped with Cu.

Quantification Report

/c:/data/Soliman21-01-2020.dset — Thu Feb 13 17:22:01 2020

State : Angle Name : Position 6

Peak	Type	Position BE (eV)	FWHM (eV)	Raw Area (cps eV)	RSF	Atomic Mass	Atomic Conc %	Mass Conc %
Ti 2p	Reg	456.000	8.926	1660981.6	2.001	47.878	22.65	49.60
C 1s	Reg	285.000	5.296	407760.0	0.278	12.011	41.34	22.71
O 1s	Reg	530.000	3.537	690190.0	0.780	15.999	24.55	17.96
F 1s	Reg	685.000	2.912	334990.0	1.000	18.998	9.51	8.26
Cu 2p	Reg	932.000	2.775	16756.7	5.521	63.549	0.09	0.27
Zn 2p	Reg	1201.000	1.000	0.0	5.589	65.387	0.00	0.00
N 1s	Reg	400.000	3.370	33403.3	0.477	14.007	1.85	1.18

Table 5 shows the Quantification report on the surface of Ti_3C_2T doped with Cu.

Quantification Report

/c:/data/Soliman21-01-2020.dset — Sun Feb 16 12:45:09 2020

State : Angle Name : Position 6

Peak	Type	Position BE (eV)	FWHM (eV)	Raw Height (cps)	RSF	Atomic Mass	Atomic Conc %	Mass Conc %
Ti 2p Ti-C 3/2	Comp	455.507	1.380	29773.0	2.001	47.878	30.02	30.02
Ti 2p Ti-O 3/2	Comp	457.486	1.770	40111.0	2.001	47.878	40.47	40.47
Ti 2p Ti-C 1/2	Comp	461.500	1.665	15966.0	2.001	47.878	16.11	16.11
Ti 2p Ti-O 1/2	Comp	463.223	1.665	15262.0	2.001	47.878	15.39	15.39

Table 6 shows the quantification report Ti 2p ratios in the as-prepared Cu/Ti_3C_2T

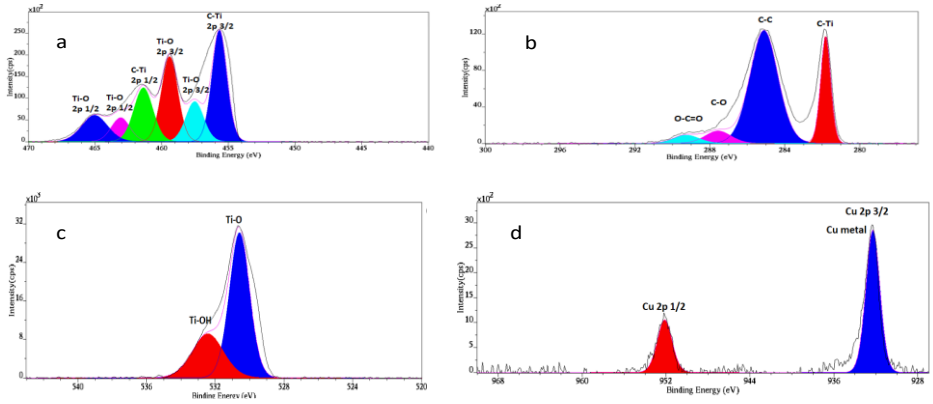

Figure 43 (a, b, c &d) The high-resolution XPS spectra of Ti 2p, C1s, O1s, and Cu 2p in the as-prepared Cu/Ti_3C_2T.

Figure 44 shows the XPS survey of the as-obtained $Cu\text{-}Zn/Ti_3C_2T$, which confirmed the presence of Ti 2p, C1s, O 1s, F1s, N1s as well as Cu 2p and Zn2p, indicates the successful doping of Ti_3C_2 with both Cu and Zn. The surface compositions revealed that the atomic content of Ti, C, O, F, Zn, and Cu are about 15.35, 50.80, 22.92, 9.52, 0.11, and 0.08, respectively as shown in (Table 7).

The high-resolution XPS spectra of Ti 2p in Cu-Zn/Ti_3C_2T sample were de-convoluted into 6 peaks, 2 peaks located at 455.7 eV for Ti $2p_{3/2}$ and at 461.4 eV for Ti $2p_{1/2}$ assigned to Ti-C along with 4 peaks at binding energies of 457.5, 459.4, 463.1, 465.06 eV for the Ti-O (Figure 45a). Likewise, the spectra of C 1s revealed 4 peaks at 281.9, 285.1, 286.7, 289.2 eV attributed to C-Ti, C-C, C-O, O-C=O, correspondingly. (Figure 45b). The high-resolution XPS spectra of O 1s were fitted into two peaks at the binding energies of 530.6 eV for Ti-O and 532.46 eV for Ti-OH (Figure 45c). The ratio of Ti-O/TiC was about 51.54/48.46 % (Table 8). The high-resolution of Zn 2p has been fitted into 2 peaks at binding energies of 1021.9 eV due to Zn $2p_{3/2}$ and 1045.1 eV due to Zn $2p_{½}$, demonstrated the presence of Zn in the metallic state (Figure 45 d). The noticed peak at 1036.3 eV may be due to Zn bonded to Ti [52]. The high resolution of Cu2p has been fitted with the main two peaks at binding energies 932.3 eV for Cu $2p_{3/2}$ and 952 eV for Cu $2p_{1/2}$, (Figure 46), indicated the successful doping with Cu.

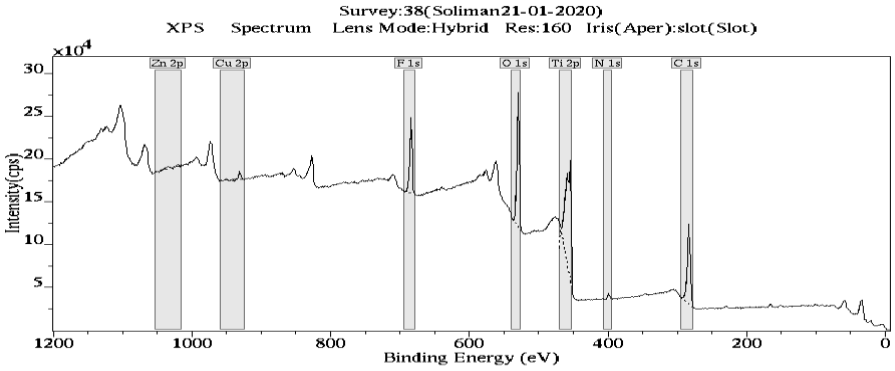

Figure 44 shows the full XPS survey of Ti_3C_2T doped with Zn and Cu

Quantification Report

/c:/data/Soliman21-01-2020.dset Thu Feb 13 17:20:51 2020

State : Angle Name : Position 4

Peak	Type	Position BE (eV)	FWHM (eV)	Raw Area (cps eV)	RSF	Atomic Mass	Atomic Conc %	Mass Conc %
Ti 2p	Reg	455.000	8.539	1142613.4	2.001	47.878	15.35	38.23
C 1s	Reg	285.000	5.001	508523.3	0.278	12.011	50.80	31.75
O 1s	Reg	530.000	3.901	653998.3	0.780	15.999	22.92	19.08
F 1s	Reg	685.000	3.466	340353.3	1.000	18.998	9.52	9.41
Cu 2p	Reg	932.000	2.902	20360.0	5.321	63.549	0.11	0.37
Zn 2p	Reg	1035.000	4.134	14288.3	5.589	65.387	0.08	0.26
N 1s	Reg	400.000	3.141	22563.3	0.477	14.007	1.23	0.90

Table 7 shows the Quantification report of Ti_3C_2T doped with Zn and Cu on the surface.

Quantification Report

/C:/data/Soliman21-01-2020.dset Sun Feb 16 12:44:44 2020

State : Angle Name : Position 4

Peak	Type	Position BE (eV)	FWHM (eV)	Raw Height (cps)	RSF	Atomic Mass	Atomic Conc %	Mass Conc %
Ti 2p Ti-C 3/2	Comp	455.700	1.320	25751.0	2.001	47.878	32.64	32.64
Ti 2p Ti-O 1/2	Comp	465.067	2.283	31349.0	2.001	47.878	39.77	39.77
Ti 2p Ti-O 3/2	Comp	457.545	1.576	9284.0	2.001	47.878	11.77	11.77
Ti 2p Ti-C 1/2	Comp	461.406	1.674	12465.0	2.001	47.878	15.81	15.81

Table 8 shows the quantification report Ti 2p ratios in the as-prepared Cu and Zn /Ti_3C_2T.

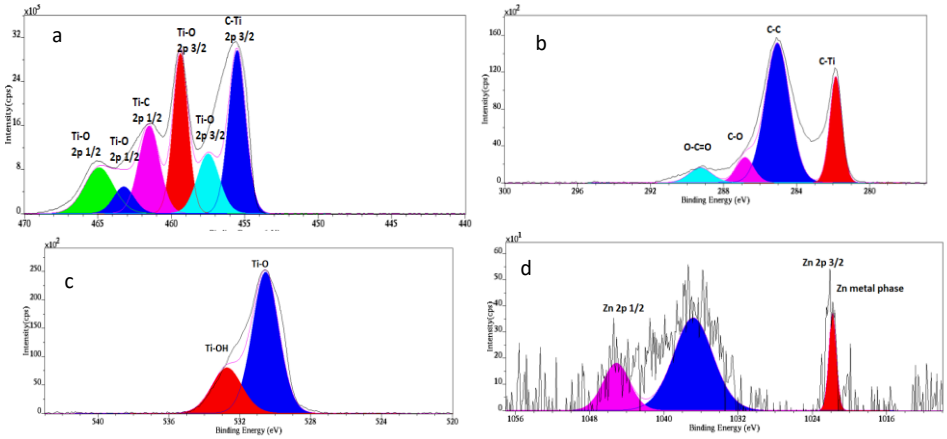

Figure 45 (a, b, c &d) The high-resolution XPS spectra of Ti 2p, C1s, O1s, and Zn 2p in the as-prepared Zn-Cu/Ti_3C_2T.

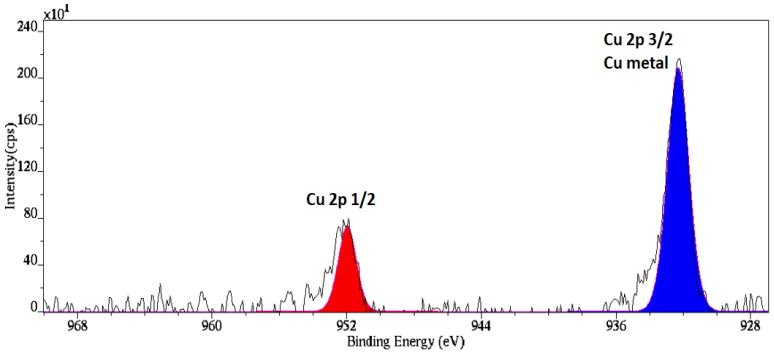

Figure 46 Shows The high-resolution XPS spectra of Cu 2p in the as-prepared Zn-Cu/Ti_3C_2T.

Electrochemical and Photoelectrochemical application

Figure 47a shows the CVs measured in CO_2 saturated an aqueous solution of 0.5 M $NaHCO_3$ at 50 mV s^{-1} at the room, on the as-synthesized Cu-Zn/Ti_3C_2T relative to Cu/Ti_3C_2T, Zn/Ti_3C_2T, and metal-free Ti_3C_2T catalysts. All materials showed the typical quasi rectangular voltammogram features of CO_2 reduction, including a reduction area with a capacitance current between from -1 V to -0.6 V and a double layer from -0.2 to 0.6 V. There are no any observed oxidation or reduction peaks for Ti, Cu, Zn and/or their oxides, indicated the stability of thus formed based materials that indicates a higher capacitance current. It is obvious that the obtained CO_2 reduction currents of Cu-Zn/Ti_3C_2T, Cu/Ti_3C_2T, and Zn/Ti_3C_2T were significantly higher than that of metal-free Ti_3C_2T catalysts, due to the doping effect with metal atoms. Noticeably, the reduction current on Cu/Ti_3C_2T (-0.15 mA cm^{-2}) was slightly higher than that of Cu-Zn/Ti_3C_2T (-0.1 mA cm^{-2}), but was significantly higher than that of Zn/Ti_3C_2T (-0.8 mA cm^{-2}) and Zn/Ti_3C_2T (-0.05 mA cm^{-2}) catalysts.

The LSV benchmarked in CO_2 saturated an aqueous solution of 0.5 M $NaHCO_3$ at 50 mV s^{-1} at room, on Cu-Zn/Ti_3C_2T compared to Cu/Ti_3C_2T, Zn/Ti_3C_2T, and metal-free Ti_3C_2T (Figure 47b). The CO_2 reduction currents on Cu-Zn/Ti_3C_3T, Cu/Ti_3C_3T, Zn/Ti_3C_2T, were superior to metal-free Ti_3C_2T under an applied voltage as indicated by the dashed lines in (Figure 47b), demonstrates their quick reduction kinetics. However, the reduction kinetics on Cu-Zn/Ti_3C_2T was greater than that of its counterpart catalysts, as indicated by its lower onset potentials, see the arrow in (Figure 47b).

Figure 47c. Displays the EIS Nyquist plots measured in CO_2 saturated 0.5 M $NaHCO_3$ at on Cu-Zn/Ti_3C_2T compared to Cu/Ti_3C_2T, Zn/Ti_3C_2T, and metal-free Ti_3C_2T under an applied potential of -0.85 V. Interestingly, both Cu-Zn/Ti_3C_2T Cu/Ti_3C_2T, and

metal-free Ti_3C_2T showed the semicircle shape while Zn/Ti_3C_2T could not, due to its high electrical resistance. Meanwhile, Cu/Ti_3C_2T showed a lower resistance than that of metal-free Ti_3C_2T, Cu-Zn/Ti_3C_2T, and Zn/Ti_3C_2T, respectively. However, at a lower frequency range, the conductivity on Cu-Zn/Ti_3C_3T was superior to all other catalysts. These results clearly warranted the quick charge transfer on Cu-Zn/Ti_3C_2T, in line with the LSV results. This is originated from the combination between the catalytic properties of metal Cu or Zn or both Cu-Zn dopants and physicochemical properties of 2D Ti_3C_2T sheets.

Figure 48a-d showed the CVs measured tested in CO_2 saturated 0.5 M $NaHCO_3$ at the room, on Cu-Zn/Ti_3C_2T compared to Cu/Ti_3C_2T, Zn/Ti_3C_2T, and metal-free Ti_3C_2T at different scan rates. The results showed the obvious increase in the current density by increasing the scan rate on all materials. The highest current density was obtained at 200 mV s^{-1} compared to 150, 100, 50, and 25 mV s^{-1}, respectively.

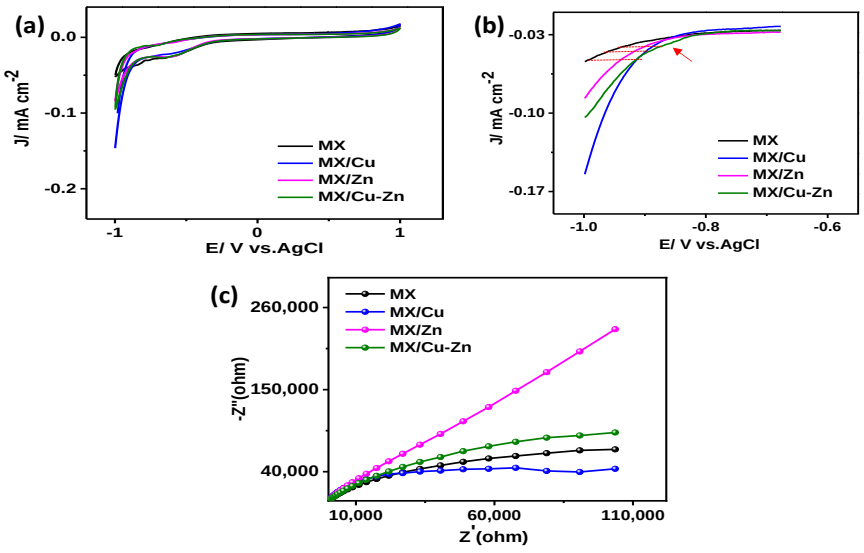

Figure 47 (a) CVs and (b) LSVs measured in CO_2 saturated an aqueous solution of 0.5 M $NaHCO_3$ under an applied potential of 20 mV s^{-1} at room temperature. (c) EIS tested in CO_2-saturated 0.5 M $NaHCO_3$ at Nyquist plots under an applied voltage of -0.85 V.

Photoelectrochemical CO_2 reduction application

The CVs were measured on the as-formed catalysts at 50 mVs-1 in CO_2 saturated o.5 M 0.5 M $NaHCO_3$ under UV-light irradiation to get more shade on the photo-electrochemical properties. The results showed that the CO_2 photocurrent density on all catalysts increased by more than 5 times under UV-light illumination. This is originated from coupling the unique electro and photo properties of Cu/Zn and Cu-Zn/Ti_3C_2T, which accelerate the charge and electron transfer under light illumination in line with elsewhere reports.[53-57].

Figure 48a-d showed the CVs tested in CO_2 saturated 0.5 M $NaHCO_3$ at the room, on Cu-Zn/Ti_3C_2T compared to Cu/Ti_3C_2T, Zn/Ti_3C_2T, and metal-free Ti_3C_2T at various scan rates under UV-light irradiation at room temperature. The results showed a substantial enhancement in the current density by increasing the scan rates on all materials. The highest obtained photocurrent density was obtained at 200 mV s^{-1} compared to 150, 100, 50, and 25 mV s^{-1}, respectively. The light enhanced the CO2 reduction of Cu/Ti_3C_2T by 10 times compared to the dark.

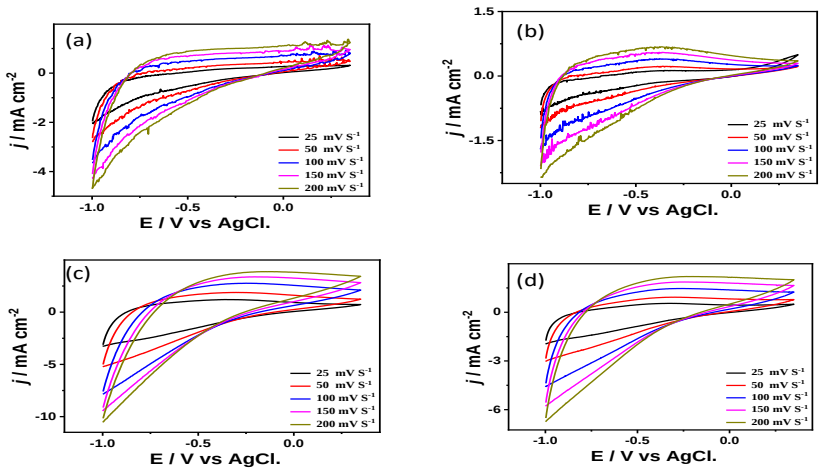

Figure 48 (a, b, c &d) Comparison voltammograms in the as-prepared Catalyst MXeneTi_3C_2T (a) ,Zn-Cu/Ti_3C_2T (b), Cu/Ti_3C_2T (c) and Zn-Cu/Ti_3C_2T (d) at different scan rate mV s−1 in CO2 -saturated 0.5 M $NaHCO_3$.(under light)

Determination of the CO_2 reduction products (electrochemical)

We have used different methods to identify the obtained products included HPLC and GC-MS; however, we could not due to the complications related to the detection of formic acid, so we have used a specific approach to detect the formic acid. The UPLC-UV- 210 nm with the assistance of the used for separation was Agilent C18 4um particle size, 4.6 x 150mm dimensions column was used for identification of the CO_2 products at ambient temperature. The mobile phase was about isocratic elution used at a constant flow rate of 1 ml/min of sulfate buffer (1 mmol/L H_2SO_4 + 8 mmol/L Na_2SO_4 (pH 2.8)). First, the calibration curve of standard formic acid was done by the by UPLC-UV/210 nm based on method LC1000 29-05, Hitachi-Technologies-corporation to ensure the formation of formic acid (Figure 49). Figure 50 shows the identification of standard formic acid with different concentrations, including 6, 61, and 122 ppm compared to a water solution at a retention time of 1.08 min. The results revealed the increase in the intensity of the formic acid peak with increasing its concentrations. Following that, the obtained solutions form the electrochemical reduction on our synthesized catalysts were estimated using the UPLC-UV-210 nm. The results displayed the presence of formic acid using Cu-Zn/Ti_3C_2T (Figure 51), Cu/Ti_3C_2T, and Zn/Ti_3C_2T. The concentrations of thus obtained formic acid were about 42.86, 42.12, and 46.56 using Cu-Zn/Ti_3C_2T, Cu/Ti_3C_2T, and Zn/Ti_3C_2T catalysts, respectively.

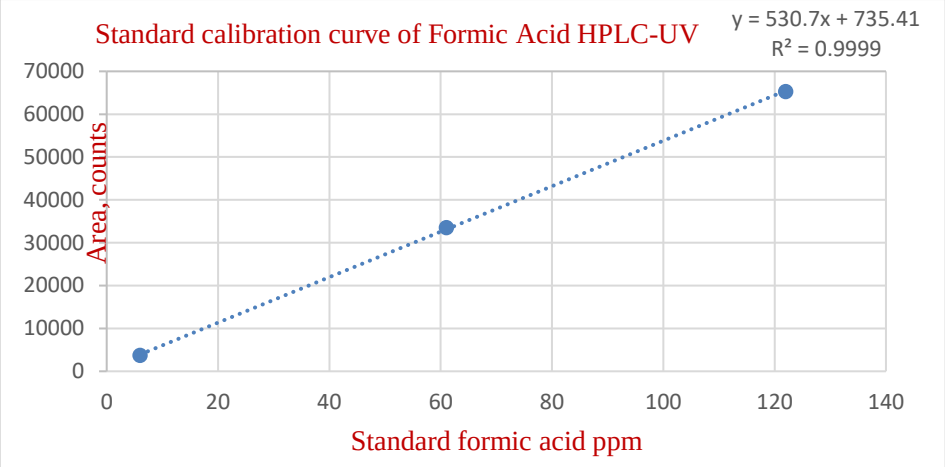

Figure 49 shows a calibration curve of standard formic acid by HPLC-UV/210 nm

Based on Sheet no –LC1000 29-05, Hitachi-Technologies-Corporation.

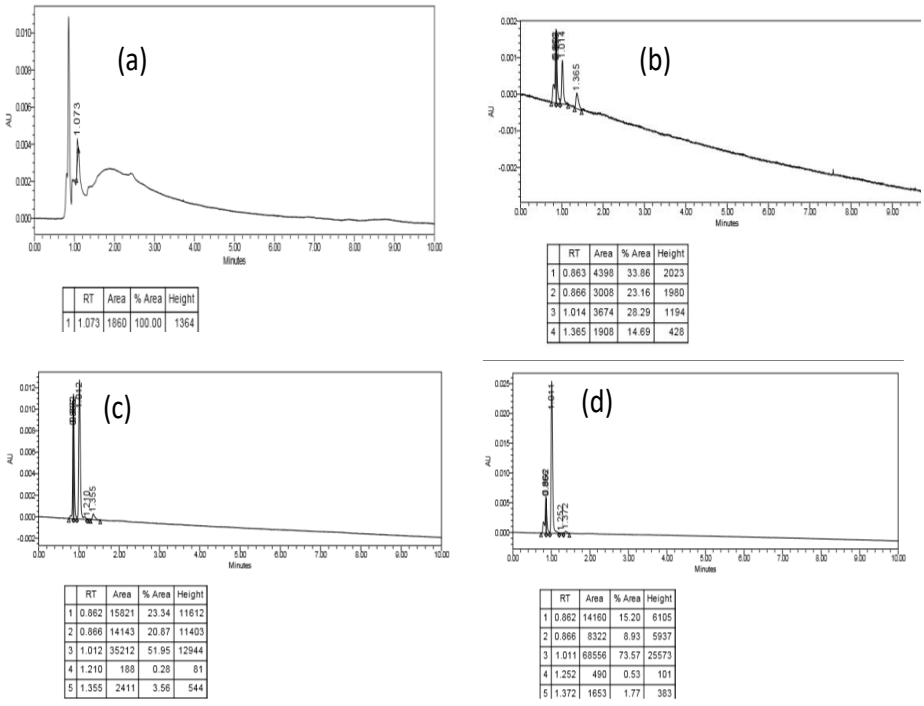

	RT	Area	% Area	Height
1	1.073	1860	100.00	1364

	RT	Area	% Area	Height
1	0.863	4398	33.86	2023
2	0.866	3008	23.16	1980
3	1.014	3674	28.29	1194
4	1.365	1908	14.69	428

	RT	Area	% Area	Height
1	0.862	15821	23.34	11612
2	0.866	14143	20.87	11403
3	1.012	35212	51.95	12944
4	1.210	188	0.28	81
5	1.355	2411	3.56	544

	RT	Area	% Area	Height
1	0.862	14160	15.20	6105
2	0.866	8322	8.93	5937
3	1.011	68556	73.57	25573
4	1.252	490	0.53	101
5	1.372	1653	1.77	383

Figure 50 (a, b, c,& d) shows the analysis of standard formic acid (6, 61 and 122 ppm) with a blank run at Rt 1.08

SAMPLE INFORMATION

Sample Name:	1C_old	Acquired By:	System
Sample Type:	Unknown	Sample Set Name:	CLU_20_134_3
Vial:	1:E,7	Acq. Method Set:	organic acids
Injection #:	1	Processing Method:	autointegration
Injection Volume:	10.00 ul	Channel Name:	PDA Ch1 210nm@4.8nm
Run Time:	10.0 Minutes	Proc. Chnl. Descr.:	PDA Ch1 210nm@4.8nm
Date Acquired:	2/3/2020 12:24:20 PM AST		
Date Processed:	2/3/2020 2:09:40 PM AST		

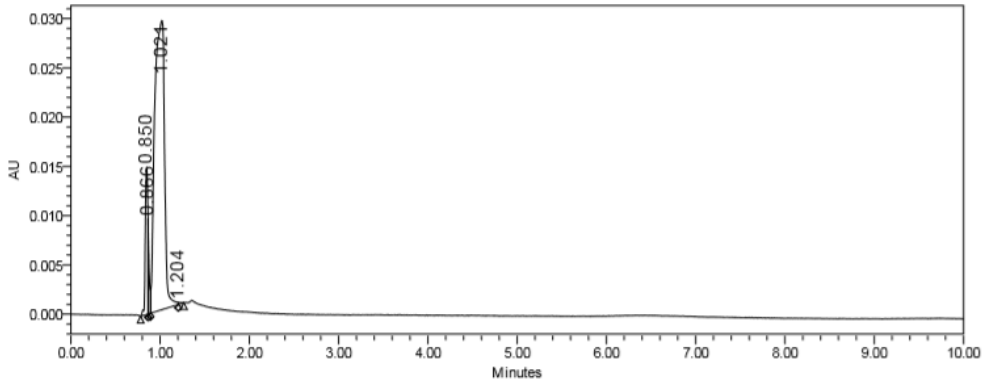

	RT	Area	% Area	Height
1	0.850	27959	10.78	14952
2	0.866	7511	2.90	9655
3	1.021	223442	86.17	29338
4	1.204	385	0.15	214

Figure 51 shows formic produced by using Ti_3C_2T/Cu &Zn sample after CO_2 reduction at RT 1.02.

4.2 CO_2 gas Conversion by using N-C-Zn capsules. (Part#2)

We have synthesized nitrogen-enriched carbon capsules doped atomically with Zn (denoted as N-C-Zn) for the thermal conversion of CO_2 reforming. Figure 52 shows the SEM images of N-C-Zn at different magnifications. It is obvious that the obtained N-C-Zn formed in a well-defined spherical shape with an average diameter of 150 nm. The spherical particles have an open pore in the range of 30 nm, as indicated by the circles in (Figure 52b), which demonstrated the formation of capsules shape. The EDX analysis reflected the presence of C, N, and Zn with atomic ratios of 86.75, 9.41, 0.1, respectively (Figure 52d).

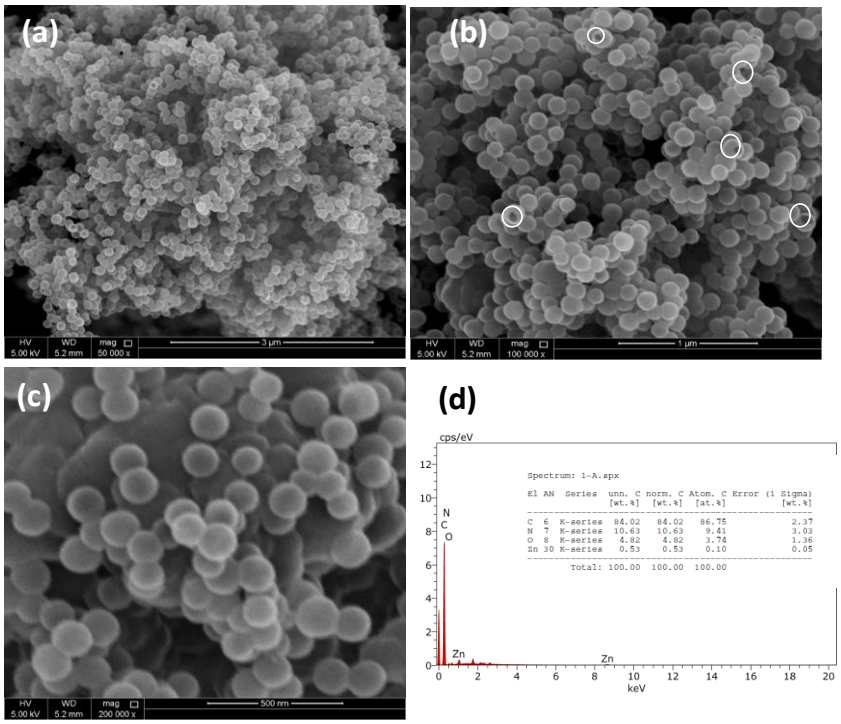

Figure 52 (a, b, c& d) Shows the SEM images and EDX analysis of the as-synthesized N-C-Zn capsules.

Figure 53a shows the XPS full survey of the as-obtained N-C-Zn capsules, which confirmed the presence of C1s, N1s, and Zn 2p. The surface compositions revealed that the atomic content of C 1s, N 1s, and Zn 2p are about 93.71, 3.46, and 0..08, respectively, as shown in (Figure 53b).

The high-resolution XPS spectra of C 1s revealed 3 peaks at 284.57, 286.2, and 288, eV attributed to C-C/C=C, and C-N, correspondingly. (Figure 54a). The high-resolution XPS spectra of N 1s were fitted into three peaks at the binding energies of 398.32, 400.7, and 403.9 eV attributed to pyridinic-N, pyrrolic-/pyridonic-N, and graphitic-type quaternary-N structure, that are the common merits for N-enriched carbon materials (Figure 54b).[58] The high-resolution spectra of Zn 2p were fitted into 4 peaks at binding energies of 1021.65 eV for Zn $2p_{3/2}$, 1044.7 Zn $2p_{½}$ as a major phase, 1024.88 eV and 1048.12 eV for ZnO as minor phase, demonstrated the presence of Zn in the metallic state (Figure 54 d).

(a)

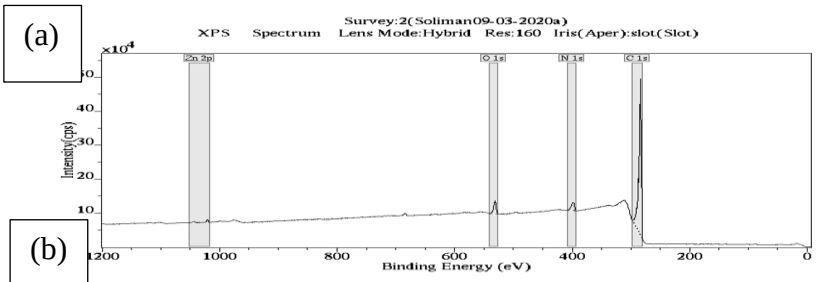

(b)

Quantification Report

/c:/data/Soliman09-03-2020a.dset Tue Mar 10 07:22:20 2020

State : Angle Name : N2-doped

Peak	Type	Position BE (eV)	FWHM (eV)	Raw Area (cps eV)	RSF	Atomic Mass	Atomic Conc %	Mass Conc %
C 1s	Reg	284.000	3.819	2219268.2	0.278	12.011	93.71	92.06
N 1s	Reg	400.000	5.938	150143.3	0.477	14.007	3.46	3.96
O 1s	Reg	532.000	4.318	186866.7	0.780	15.999	2.77	3.62
Zn 2p	Reg	1021.000	2.947	29456.7	5.589	65.387	0.07	0.36

Figure 53 (a &b) XPS full survey and quantification report on the surface in the as- of the as-synthesized N-C-Zn capsules.

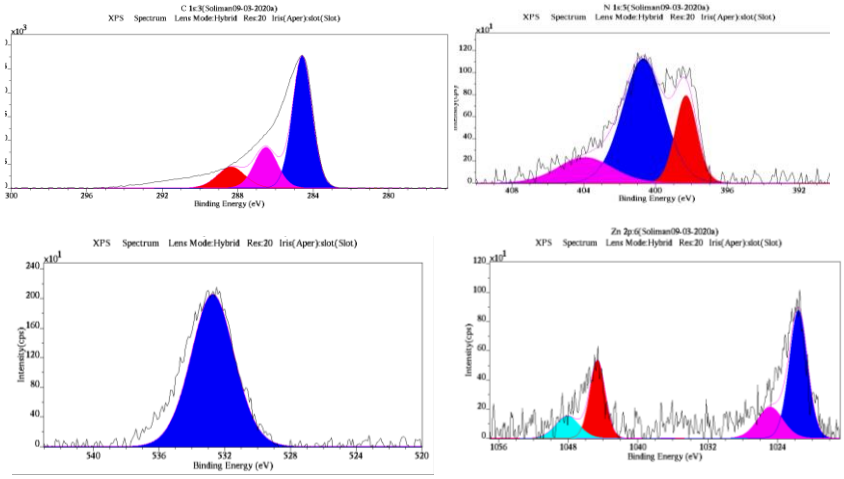

Figure 54 (a, b, c &d). The high-resolution XPS spectra of C 1s, N 1s, O 1s, and Zn 2p in the of the as-synthesized N-C-Zn capsules (Fresh sample).

Figure 55 shows the XRD analysis of the as-synthesized N-C-Zn capsules, which depicted the presence of one broad diffraction pattern at 27º assigned to {002} facet and a small peak at 43º attributed to the {100} facet of graphic carbon.

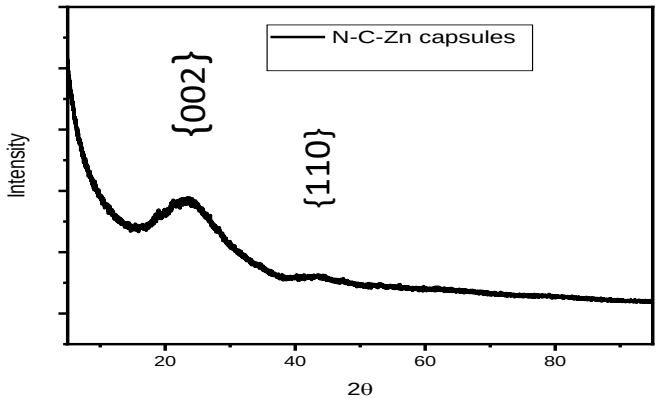

Figure 55 displays the XRD spectra of N-C-Zn capsules.

Figure 56 shows the TGA of N-C-Zn capsules carried out under nitrogen while heating from room temperature until 900 º at a heating rate of 5 ºC min. The results showed the great thermal stability of N-C-Zn capsules without any significant decomposition until 624.78 ºC. The formation of stable thermal catalysts is highly preferred in the large-scale and practical gas reforming applications.

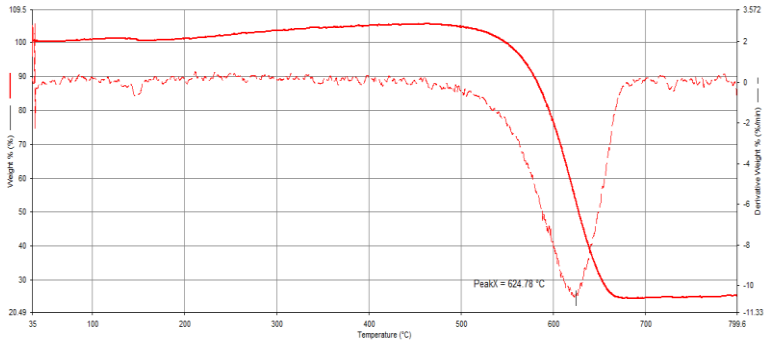

Figure 56 shows that the decomposition temperature of the as-synthesized N-C-Zn capsules.

The N_2-isotherm adsorption/desorption analysis was measured on N-C-Zn capsules, and the surface area was clouted using the Brunauer-Emmett-Teller (BET) method, and the pore volume was calculated using the Barrett-Joyner-Halenda (BJH) method. The N2-isotherm features close to the IV type curve with an H_4 hysteresis loop with 2 obvious steps capillary steps in the range of P/Po < 0.5 and P/Po > 0.9 (Figure 57). This is ensuring the formation of capsules with multiple pores, including meso, micro, and macropore. The estimated BET surface area was found to be 245.78 m^2 g^{-1}, and the pore volume 1.12 cc/g."

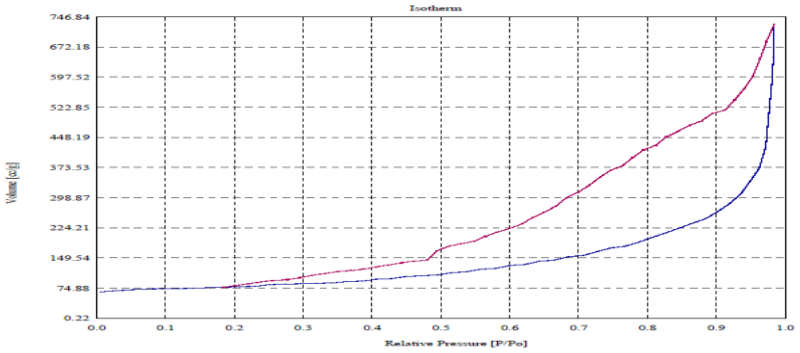

Figure 57. N_2 isotherm adsorption/desorption curve on N-C-Zn capsules.

CO_2 conversion /N-C-Zn capsules Application ad Products (catalytic conversion).

The thermal CO_2 reforming was carried out on the as-made N-C-Zn capsules in a Fixed-bed reactor at different temperatures from 200 ^oC to 300 ^oC and pressures from 1 bar to 50 bar. The reaction was measured 100 mg of N-C-Zn capsules under a continuous flow of CO_2/H_2 wit a ratio of 3/1 with a total flow of 65 mL/min inside the fixed-bed reactor connected to an online GC-TCD (Agilent, USA) The results were recorded every 20 min interval. Figure 58 a-d shows the reaction products obtained at different pressures, including 1, 10, 20, and 40 bar at 300 ^oC. The results demonstrated the formation of CO, CH_4, and C_2H_5. Figure 59 showed the CO_2 reforming selectivity as a function of pressures. Intriguingly enough, at 1 bar, the N-C-Zn capsules showed the selective reforming into CO with an average conversion of 78 %. Meanwhile, with increasing the pressure, the CH_4 yield increases significantly from 20 % at 1 bar to 70 % at 40 bar, whereas the yield of C_2H_5 also increased slightly with increasing the pressure.

Figure 60 shows the CO2 reforming on N-C-Zn capsules carried out at differing temperatures ranged from 200 ^oC to 300 ^oC at 1 bar. Intriguingly, at 200 C, the CO yield was in the range of 50 % volume, while the CO yield decreased significantly with increasing the temperatures. However, both CH_4 and C_2H_5 increased with increasing temperatures. The low yield of both CH_4 and C_2H_5 at low temperatures due to the difficulties related to the adsorption of CO_2 at low pressure.

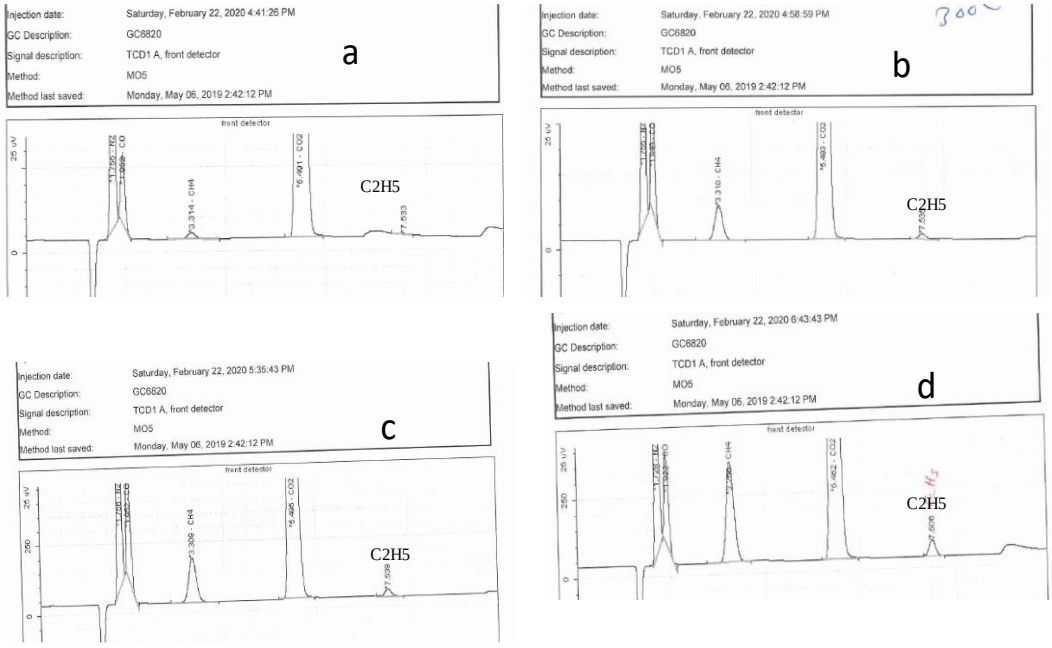

Figure 58 Agilent GC-TCD chromatogram shows CO, N, CH4, CO2 &C2H5 compounds.

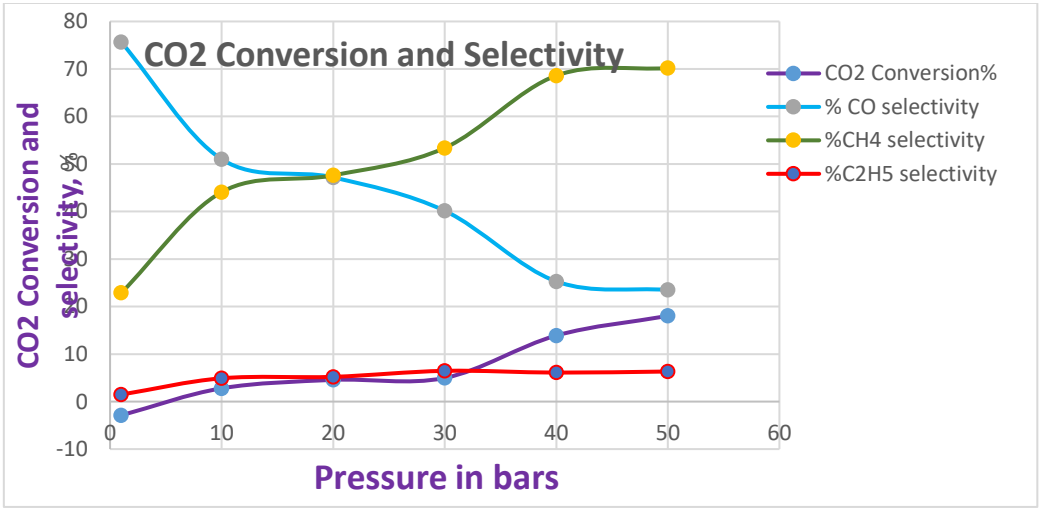

Figure 59 Shows Thermal CO2 Conversion and Selectivity using N-C-Zn capsules at a fixed temperature.

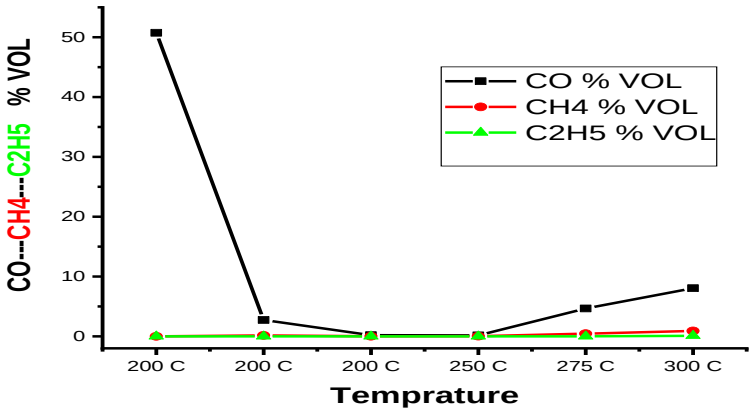

Figure 60 shows that high CO produced at 0-time reaction at atmospheric pressure.

after10 min reaction at the same temperature 200 °C, the CO has been reduced, unlike the CH4 and C2H5 increased by increasing Temperature & the time of reaction at atmospheric pressure.

Chapter 5: Conclusion and future prospective.

In summary, to give synopsis briefly on the relevant millstone of this thesis rooting from the literature view until the results as well as the future prospective.

The fabrication of efficient and low-cost catalysts for gas conversion reactions has attracted much great attention in the last few decades. However, there still some fences related to the high temperature, high pressure, and the high cost of the catalysts. So, based on the literature review carried out via all the databases, we have selected MXene and carbon capsules materials because of the rare reports on the utilization of these materials in the gas conversion reaction.

We have prepared two novel catalysts, including MXene 2D sheets doped with Cu, Zn, and Cu-Zn at the atomic level for CO_2 reduction via the electrochemical, photo-electrochemical approaches. The obtained materials were analyzed using SEM, TEM, EDX, XRD, and XPS, which all showed the successful formation of 2D sheets doped

with Cu (Cu/Ti_3C_2T) or Zn (Zn/Ti_3C_2T) and crumbed ultrathin sheets doped with Cu and Zn ($Cu\text{-}Zn/Ti_3C_2T$). The atomic doping enhanced the CO_2 electrochemical reduction performance significantly compared to metal-free Ti_3C_2T. Noticeably, Cu/Ti_3C_2T showed higher catalytic activity than $Cu\text{-}Zn/Ti_3C_2T$ and Zn/Ti_3C_2T. Interestingly, the UV-light irradiation enhanced the CO2 reduction activity by 5 times compared to under dark. All the synthesized catalysts allowed the selective CO_2 reduction to formic acid.

The second novel catalysts were nitrogen-enriched carbon capsules doped atomically with Zn (N-C-Zn). The shape and composition of N-C-Zn capsules were confirmed by the SEM, XRD, XPS, BET, BJH, and TGA. The capsules shape with an average diameter of 150 nm and an average pore volume of 1.1 cc/g, surface area 245.78 m2 g-1 and enriched with N (9.41 %) and doped atomically with Zn (0.1). The thermal CO_2/H_2 reforming was estimated at different temperatures and pressures. The results showed the selective production of CO at 200 ^oC under, while the CO decreased with increasing temperature to 300 ^oC and pressure to 40 bar, contrarily the production of CH_4 increased significantly to reach 70 % with increasing pressure to 40 bar. Meanwhile, the formation of C_2H_5 slightly increased with increasing the pressure.

In the future prospective, there is a critical need to further develop novel methods for characterization of carbon-based materials doped atomically with metal atoms to understand and to tailor their properties for CO_2 conversion reactions under a temperature lower than 150 ^oC as recommended by the department of energy, USA to achieve sustainable future. Also, the fabrication process of carbon-based materials need additional improvement.

Chapter 6: References

1. Royer, S. and D. Duprez, *Catalytic oxidation of carbon monoxide over transition metal oxides.* ChemCatChem, 2011. **3**(1): p. 24-65.
2. Khalil, M.A.K. and R.A. Rasmussen, *Carbon monoxide in the Earth's atmosphere: Indications of a global increase.* Nature, 1988. **332**(6161): p. 242.
3. Li, X., et al., *Cocatalysts for Selective Photoreduction of CO_2 into Solar Fuels.* Chem. Rev., 2019. **119**(6): p. 3962-4179.
4. Eid, K., M.H. Sliem, and A.M. Abdullah, *Unraveling Template-free Fabrication of Carbon Nitride Nanorods Codoped with Pt and Pd for Efficient Electrochemical and Photoelectrochemical Carbon Monoxide Oxidation at Room Temperature.* Nanoscale, 2019.
5. Liu, T., et al., *Preparation and Evaluation of Copper–Manganese Oxide as a High-Efficiency Catalyst for CO Oxidation and NO Reduction by CO.* J. Phys. Chem. C, 2017. **121**(23): p. 12757-12770.
6. Guo, C., et al., *Initial Reduction of CO_2 on Pd-, Ru-, and Cu-Doped CeO_2(111) Surfaces: Effects of Surface Modification on Catalytic Activity and Selectivity.* ACS Appl. Mater. Interfaces, 2017. **9**(31): p. 26107-26117.
7. Barrio, J., et al., *Unprecedented Centimeter-Long Carbon Nitride Needles: Synthesis, Characterization and Applications.* Small, 2018. **14**(21): p. 1800633.
8. Liu, J.-X., et al., *A Linear Scaling Relation for CO Oxidation on CeO_2-Supported Pd.* J. Am. Chem. Soc., 2018. **140**(13): p. 4580-4587.
9. Spronsen, M.A.v., J.W.M. Frenken, and I.M.N. Groot, *Surface science under reaction conditions: CO oxidation on Pt and Pd model catalysts.* Chem. Soc. Rev., 2017. **46**(14): p. 4347-4374.
10. Hu, S., et al., *Molecular O_2 Activation over Cu(I)-Mediated C≡N Bond for Low-*

Temperature CO Oxidation. ACS Appl. Mater. Interfaces, 2018. **10**(20): p. 17167-17174.

11. Heo, I., et al., *Improved thermal stability of a copper-containing ceria-based catalyst for low temperature CO oxidation under simulated diesel exhaust conditions.* Catal. Sci. Technol., 2018. **8**(5): p. 1383-1394.
12. Liu, X., et al., *Bifunctional CO oxidation over Mn-mullite anchored Pt sub-nanoclusters via atomic layer deposition.* Chem. Sci., 2018. **9**(9): p. 2469-2473.
13. Wei, S., et al., *Au/TiO_2 Catalysts for CO Oxidation: Effect of Gold State to Reactivity*. J. Phys. Chem. C, 2018. **122**(9): p. 4928-4936.
14. Xu, J., et al., *Biphasic Pd−Au Alloy Catalyst for Low-Temperature CO Oxidation.* J. Am. Chem. Soc., 2010. **132**(30): p. 10398-10406.
15. Ma, S., et al., *Electroreduction of Carbon Dioxide to Hydrocarbons Using Bimetallic Cu–Pd Catalysts with Different Mixing Patterns.* J. Am. Chem. Soc., 2017. **139**(1): p. 47-50.
16. Zhang, W., et al., *Origin of Enhanced Activities for CO Oxidation and O_2 Reaction over Composition-Optimized $Pd_{50}Cu_{50}$ Nanoalloy Catalysts.* J. Phys. Chem. C, 2017. **121**(20): p. 11010-11020.
17. Januszewska, A., R. Jurczakowski, and P.J. Kulesza, *CO_2 Electroreduction at Bare and Cu-Decorated Pd Pseudomorphic Layers: Catalyst Tuning by Controlled and Indirect Supporting onto Au(111).* Langmuir, 2014. **30**(47): p. 14314-14321.
18. Long, R., et al., *Isolation of Cu Atoms in Pd Lattice: Forming Highly Selective Sites for Photocatalytic Conversion of CO_2 to CH_4.* J. Am. Chem. Soc., 2017. **139**(12): p. 4486-4492.
19. Liu, L., et al., *Mechanistic Study of Pd–Cu Bimetallic Catalysts for Methanol*

Synthesis from CO_2 Hydrogenation. J. Phys. Chem. C, 2017. **121**(47): p. 26287-26299.

20. Jin, M., et al., *Low-temperature CO oxidation over Pd catalysts supported on highly ordered mesoporous metal oxides.* Catal. Today, 2012. **185**(1): p. 183-190.

21. Zhai, X., et al., *TiO_2-nanosheet-assembled microspheres as Pd-catalyst support for highly-stable low-temperature CO oxidation.* New J. Chem., 2018. **42**(22): p. 18066-18076.

22. Ma, D., et al., *3d transition metal embedded C_2N monolayers as promising single-atom catalysts: A first-principles study.* Carbon, 2016. **105**: p. 463-473.

23. Liang, H.-W., et al., *Hierarchically porous carbons with optimized nitrogen doping as highly active electrocatalysts for oxygen reduction.* Nat. Commun., 2014. **5**: p. 4973.

24. Wang, S., et al., *Confined Catalysis in the g-C_3N_4/Pt (111) Interface: Feasible Molecule Intercalation, Tunable Molecule–Metal Interaction, and Enhanced Reaction Activity of CO Oxidation.* ACS Appl. Mater. Interfaces, 2017. **9**(38): p. 33267-33273.

25. Eid, K., et al., *Versatile Synthesis of Pd and Cu Co-Doped Porous Carbon Nitride Nanowires for Catalytic CO Oxidation Reaction.* Catalysts, 2018. **8**(10): p. 411.

26. Eid, K., et al., *Precise fabrication of porous one-dimensional gC3N4 nanotubes doped with Pd and Cu atoms for efficient CO oxidation and CO2 reduction.* Inorganic Chemistry Communications, 2019. **107**: p. 107460.

27. Eid, K., et al., *Rational synthesis of one-dimensional carbon nitride-based nanofibers atomically doped with Au/Pd for efficient carbon monoxide*

oxidation. International Journal of Hydrogen Energy, 2019.

28. Eid, K., et al., *Data on structural and composition-related merits of gC3N4 nanofibres doped and undoped with Au/Pd at the atomic level for efficient catalytic CO oxidation.* Data in brief, 2019. **27**: p. 104734.
29. Eid, K. and A.M. Abdullah, *Data on the catalytic CO oxidation and CO2 reduction durability on gC3N4 nanotubes Co-doped atomically with Pd and Cu.* Data in brief, 2019. **26**: p. 104495.
30. JIULONG, S., *DEVELOPMENT OF INORGANIC-ORGANIC HYBRID MATERIALS FOR WASTE WATER TREATMENT*. 2014.
31. Guettel, R. and T.J.C.E.S. Turek, *Comparison of different reactor types for low temperature Fischer–Tropsch synthesis: a simulation study.* 2009. **64**(5): p. 955-964.
32. Inglezakis, V., S.J.A. Poulopoulos, Ion Exchange, and F.E. Catalysis", Elsevier, Amsterdam, The Netherlands, *Heterogeneous Processes and Reactor Analysis.* 2006: p. 148-160.
33. https://knoema.com/atlas/ranks/CO2-emissions-per-capita?action=export&gadget=tranking-container.
34. Jhong, H.R.M., et al., *A nitrogen-doped carbon catalyst for electrochemical CO2 conversion to CO with high selectivity and current density.* 2017. **10**(6): p. 1094-1099.
35. Varela, A.S., et al., *Electrochemical Reduction of CO2 on Metal-Nitrogen-Doped Carbon Catalysts.* 2019. **9**(8): p. 7270-7284.
36. Ma, C., et al., *Carbon nanotubes with rich pyridinic nitrogen for gas phase CO2 electroreduction.* 2019. **250**: p. 347-354.
37. Zhang, L., et al., *N-doped porous carbon-encapsulated Fe nanoparticles as*

efficient electrocatalysts for oxygen reduction reaction. 2018. **445**: p. 462-470.

38. Jia, C., et al., *Carbon-based catalysts for electrochemical CO 2 reduction.* 2019. **3**(11): p. 2890-2906.

39. Zeng, Z., et al., *Boosting the photocatalytic ability of Cu2O nanowires for CO2 conversion by MXene quantum dots.* 2019. **29**(2): p. 1806500.

40. Cao, S., et al., *2D/2D heterojunction of ultrathin MXene/Bi2WO6 nanosheets for improved photocatalytic CO2 reduction.* 2018. **28**(21): p. 1800136.

41. Low, J., et al., *TiO2/MXene Ti3C2 composite with excellent photocatalytic CO2 reduction activity.* 2018. **361**: p. 255-266.

42. Zhao, D., et al., *MXene (Ti3C2) vacancy-confined single-atom catalyst for efficient functionalization of CO2.* 2019. **141**(9): p. 4086-4093.

43. Eid, K., et al., *Versatile Synthesis of Pd and Cu Co-Doped Porous Carbon Nitride Nanowires for Catalytic CO Oxidation Reaction.* Catalysts, 2018. **8**(10).

44. Eid, K., et al., *Rational Synthesis of Porous Graphitic-like Carbon Nitride Nanotubes Codoped with Au and Pd as an Efficient Catalyst for Carbon Monoxide Oxidation.* Langmuir, 2019. **35**(9): p. 3421-3431.

45. Mukri, B.D., U.V. Waghmare, and M.J.C.o.M. Hegde, *Platinum Ion-Doped TiO2: High Catalytic Activity of Pt2+ with Oxide Ion Vacancy in Ti4+ 1–x Pt2+ x O2–x Compared to Pt4+ without Oxide Ion Vacancy in Ti4+ 1–x Pt4+ x O2.* 2013. **25**(19): p. 3822-3833.

46. Bera, P., et al., *Ionic dispersion of Pt and Pd on CeO2 by combustion method: effect of metal–ceria interaction on catalytic activities for NO reduction and CO and hydrocarbon oxidation.* 2000. **196**(2): p. 293-301.

47. Eid, K., et al., *Rational synthesis of one-dimensional carbon nitride-based nanofibers atomically doped with Au/Pd for efficient carbon monoxide*

oxidation. 2019. **44**(33): p. 17943-17953.

48. Eid, K., et al., *Rational synthesis of porous graphitic-like carbon nitride nanotubes codoped with Au and Pd as an efficient catalyst for carbon monoxide oxidation.* 2019. **35**(9): p. 3421-3431.

49. Eid, K., M.H. Sliem, and A.M.J.N. Abdullah, *Unraveling template-free fabrication of carbon nitride nanorods codoped with Pt and Pd for efficient electrochemical and photoelectrochemical carbon monoxide oxidation at room temperature.* 2019. **11**(24): p. 11755-11764.

50. Peterson, E.J., et al., *Low-temperature carbon monoxide oxidation catalysed by regenerable atomically dispersed palladium on alumina.* 2014. **5**(1): p. 1-11.

51. Li, Y., et al., *Ti3C2 MXene-derived Ti3C2/TiO2 nanoflowers for noble-metal-free photocatalytic overall water splitting.* 2018. **13**: p. 217-227.

52. Zhu, Z., et al., *Photocatalytic performances and activities in Ag-doped ZnAl 2 O 4 nanorods studied by FTIR spectroscopy.* 2013. **3**(3): p. 788-796.

53. Reñones, P., et al., *Hierarchical TiO2 nanofibres as photocatalyst for CO2 reduction: Influence of morphology and phase composition on catalytic activity.* 2016. **15**: p. 24-31.

54. Li, X., et al., *Cocatalysts for selective photoreduction of CO2 into solar fuels.* 2019. **119**(6): p. 3962-4179.

55. Kim, H.R., et al., *Heterojunction pnp Cu2O/S-TiO2/CuO: Synthesis and application to photocatalytic conversion of CO2 to methane.* 2017. **20**: p. 91-96.

56. Lashgari, M., S. Soodi, and P.J.J.o.C.U. Zeinalkhani, *Photocatalytic back-conversion of CO2 into oxygenate fuels using an efficient ZnO/CuO/carbon*

nanotube solar-energy-material: Artificial photosynthesis. 2017. **18**: p. 89-97.

57. Guo, Q., et al., *Improved photocatalytic activity of porous ZnO nanosheets by thermal deposition graphene-like g-C3N4 for CO2 reduction with H2O vapor.* 2020. **509**: p. 144773.

58. Feng, S., et al., *Synthesis of nitrogen-doped hollow carbon nanospheres for CO 2 capture.* 2014. **50**(3): p. 329-331.